Final Report

Project Title:	Improved Performance of $Cu(InGa)(SeS)_2$ PV Modules using the Reaction of Metal Precursors
Project Period:	09/01/16 – 02/29/20
Project Budget:	$888,889
Submission Date:	12/15/20
Recipient:	Institute of Energy Conversion, University of Delaware
Address:	451 Wyoming Rd. Newark, DE 19716
Award Number:	DE-EE00007542
Project Team:	University of Delaware Columbia University Lawrence Berkeley National Lab

Contacts:

William Shafarman	Susan Tompkins
Principal Investigator	Business Contact
302-831-6215	302-831-8002
wns@udel.edu	sdt@udel.edu

Acknowledgment: This material is based upon work supported by the Department of Energy, Office of Energy Efficiency and Renewable Energy, Solar Energy Technologies Office, under Award Number DE-EE0007542.

Disclaimer: This report was prepared as an account of work sponsored by an agency of the United States Government. Neither the United States Government nor any agency thereof, nor any of their employees, makes any warranty, express or implied, or assumes any legal liability or responsibility for the accuracy, completeness, or usefulness of any information, apparatus, product, or process disclosed, or represents that its use would not infringe privately owned rights. Reference herein to any specific commercial product, process, or service by trade name, trademark, manufacturer, or otherwise does not necessarily constitute or imply its endorsement, recommendation, or favoring by the United States Government or any agency thereof. The views and opinions of authors expressed herein do not necessarily state or reflect those of the United States Government or any agency thereof.

Executive Summary

This project "Improved Performance of $Cu(InGa)(SeS)_2$ PV Modules using the Reaction of Metal Precursors", a partnership led by the Institute of Energy Conversion (IEC) at the University of Delaware with Columbia University and the Molecular Foundry at the Lawrence Berkeley National Laboratory, aimed to develop pathways to improve $Cu(InGa)(SeS)_2$ (CIGSS) thin film photovoltaic modules using processes compatible with low manufacturing cost. The CIGSS approach investigated was a two-step process including sputter deposition of metal precursor films following by reaction in hydride gases utilizing IEC's novel H_2Se/ H_2S reactor. The multi-step batch reaction was similar to that under commercial development by the project's industry partner Stion. When Stion went out of business mid-project the focus changed to a rapid thermal process (RTP) considered more commercially viable.

Approaches to improve the performance and particularly open circuit voltage (V_{OC}) of reacted films focused on two material innovations: (1) increasing the overall Ga content and effective bandgap to increase V_{OC}, and (2) investigating processing and performance advantages arising from Ag alloying. Advanced characterization including photoluminescence and device analysis and simulation were used to guide process and material development including control of relative composition gradients.

Research on the formation of Cu-Ga-In metal precursors resulted in processes for deposition of precursor stacks with the Ga/(In+Ga) ratio was increased from the typical ratio 0.25, limited by availability of alloy sputter targets, to 0.5. Effects of sputter parameters, especially for the elemental In layer, on morphology and phase composition were established. It was shown that, after annealing, precursor films with Ga/(In+Ga) in the range 0.25 – 0.5 have comparable phase composition and morphology so subsequent reaction follows from the same starting point. The addition of Ag to the precursors gave more uniform morphology and improved adhesion of reacted films which enable higher reaction temperature for faster processing. A novel outcome was the discovery of a new quaternary Laves-type phase in sputter-deposited and evaporated Ag-Cu-In-Ga thin films.

Hydride gas reaction processes including time-temperature-concentration profiles were developed for different precursor compositions. This enables control of composition profiles to engineer through-film bandgap gradients including sufficient Ga content near the front of the film where it's needed to increase V_{OC}. Device characterization and simulations were used to correlate measured film composition profiles to J-V and QE measurements of devices and guide optimization of composition and bandgap gradients. In particular, the S gradient at the front of the CIGSS film was found to be critical to controlling current collection and recombination. The simulations guided process development leading to improved reproducibility of devices with Ga/(In+Ga) = 0.25 and improved performance with Ga/(In+Ga) = 0.4 – 0.5. This process development led to a validation that increased Ga in the precursor could be utilized to increase V_{OC} with an 80 mV gain achieved by increasing the precursor composition from Ga(In+Ga) from 25 to 50%. With an intermediate 40% Ga ratio, 16.0 % device conversion efficiency matched that with the lower Ga baseline cells even with 50 mV increase in V_{OC}.

With Ag-alloyed precursors, the reaction pathways leading from intermetallic phases to $(AgCu)(InGa)(SeS)_2$ (ACIGSS) were determined. A significant finding was that Ag-alloying increases the reaction rate to completely convert precursor films to the final chalcopyrite which could enable reduced reaction time to benefit manufacturability.

To maintain potential commercial viability, the process under investigation was refocused to an RTP reaction that could potentially be incorporated into an in-line process. Precursors with different composition were capped with a Se layer and reacted in H_2S for 5-15 minutes, compared to typically 2 hours in the previous multi-step batch process. Critical RTP parameters were identified including the Se layer thickness to control competing reaction and evaporation of Se, substrate temperature ramp rates, and the temperature uniformity of the substrate. Processes were developed to control reaction with different precursor compositions and specifically to control S incorporation. Devices produced with RTP did not achieve comparable performance to films produced with long reactions, limited partly by non-uniformity arising from small variations in the RTP heating. But pathways to high quality devices with further optimization and improved heating uniformity were developed.

The project developed new optoelectronic characterization approaches with a focus on development and application of spatial- and time-resolved photoluminescence and a custom IR microscope for mapping photoluminescence and carrier lifetime of CIGS materials was built. It was shown that minority carrier lifetime strongly depends on the chemical composition and general quality of the material and that a wide range of samples show inhomogeneity of carrier lifetime on the length scale of 2-7 µm. Additionally, two-photon excitation capability was developed to utilize differences in excitation-emission for distinguishing bulk vs surface lifetime in CIGS films.

The project advances the state-of-the -art for precursor reaction processes in several ways that coiuld impact manufacturing. This includes the validation of increased Ga in the precursor to increase V_{OC} and the establishment of model-guided control to form optimal composition profiles. The application of these process control approaches to batch and RTP processes increases their potential impact although only the latter now seems to be possibly commercially viable. Potential benefits of Ag-alloying to increase reaction rates and improve adhesion were also demonstrated. In all cases, knoowledge of precursor phase formation and reaction pathways to form chalcogenide alloy phases can be critically valuable in designing a large-scale process. Finally, progress in photoluminescence-based characterization has highlighted new approaches to identify non-homogeneities and separate losses that might affect device performance with CIGSS.

Table of Contents

Executive Summary 2
Table of Contents 4
Background 5
Introduction 6
Project Results and Discussion 9
I. Alloying and increased bandgap 9
II. Composition and surface control 18
III. Materials characterization 32
Conclusions 42
Budget and Schedule 44
Path Forward 44
Publications Resulting from This Work 45
Acknowledgments 45
References 46

Background

The primary objective of this project was to develop pathways to improve $Cu(InGa)(SeS)_2$ (CIGSS) modules using precursor reaction processes compatible with low manufacturing cost. The precursor reaction selenization/sulfization process is typically a two-step reaction process[1] often referred to as SAS for sulfization after selenization. This approach to absorber processing includes the deposition of a Cu-In-Ga metal precursor stack, typically deposited by sputtering, followed by reaction in H_2Se and H_2S gases. This sequential process with reaction in H_2Se at 400 – 450°C followed by reaction in H_2S at 500-600°C was developed by Siemens/Shell Solar and Showa Shell[2] and is used in large-scale manufacturing. Currently, Solar Frontier is producing ~ 1GW/year using CIGSS technology and has made remarkable progress in raising the performance of cells and pilot-scale modules. This now includes a world record small area cell with 23.4% efficiency[3]. These cells, as well as module results reported by Samsung and TSMC use high strain point glass substrates that allows process temperatures ~ 600°C even on m^2 scale glass substrates[4]. In addition, they typically have relatively low $V_{OC} \leq 700$ mV compared to high efficiency devices with co-evaporated CIGS. The project's approaches to improve the performance and specifically open circuit voltage of reacted films focused on two material innovations: (1) increasing the overall Ga content from Ga/(In+Ga) ≈ 0.25 as used typically in this process to 0.5 to form reacted films with higher bandgap and V_{OC}, and (2) investigating processing and performance advantages arising from Ag alloying. Fundamental characterization of optoelectronic film properties and advanced device models were used to guide development of H_2Se/H_2S reaction processes including control of relative Ga/In and S/Se profiles for reduced recombination.

Critical technical issues with the precursor reaction process include control of the through-film composition, with Ga accumulation at the back of the reacted film resulting in low bandgap near the front. This is a reason for lower voltage devices. Incorporation of higher overall Ga content is limited for practical reasons as the preferred method for sputtering the precursors utilizes Cu_3Ga and In sputter targets. Cu-Ga targets with higher Ga content are difficult to manufacture and are not readily available. The reactions also include a S-reaction at the end of the process. S increases the bandgap in the near surface region, which is critical to preventing a loss in V_{OC} by additional recombination in this region of the absorber[5]. Other issues specific to the process include the formation of voids in the absorber films[6] and poor adhesion at the Mo/CIGSS interface[5].

In the last few years including the period of performance of this project it became clear that the most common manufacturing approach to precursor reaction of CIGSS could no longer be considered commercially viable. In particular, this project was established with a commercial partner, Stion, who had a manufacturing facility making modules in Mississippi and was keenly interested in partnering to develop approaches to improve the performance of their CIGSS. However, during the project Stion went out of business. This followed the decisions of two major potential manufacturers in Asia, Samsung and TSMC, to cease pilot production of CIGSS using similar processes despite substantial investments in manufacturing development. Finally, Solar Frontier revealed in 2018 during the course of the project that they changed their approach from a batch process similar to that used in this project and at Stion to an in-line rapid thermal process (RTP)[7]. They have reported significant progress at the cell and sub-module levels including the

fabrication of record efficiencies[3] but they have not reported progress in the performance or additional scale-up of their manufacturing of large area modules.

One other manufacturer, Avancis, also uses an RTP process with Se-capped sputtered precursors[8]. They have reported progress recently on development of novel Cd-free buffer layers[9]. They are also reportedly partnering with CNBR (China National Building Materials) to build a manufacturing capacity in China with a market focus on building integrated applications. A relevant feature of their process is relatively low V_{OC} attributed to Ga segregation toward the back of the absorber which is addressed in the objectives of this project.

Introduction

The most successful method for commercial production of $Cu(InGa)(SeS)_2$ (CIGSS) thin film photovoltaics was based on absorber formation by a two-step precursor reaction process with ~1GW/yr scale production by Solar Frontier. DC sputtering is commonly used for the precursor deposition because it is scalable using commercially available deposition technology that is already used for the Mo back contact. The reaction has typically used a two-step process with reaction in H_2Se followed by reaction in H_2S. An alternative process starts with an elemental Se layer deposited on the metal precursor followed by reaction in H_2S. This project aims to improve the performance of thin film $Cu(InGa)(SeS)_2$ (CIGSS) PV on inexpensive soda lime glass substrates by developing innovative approaches for deposition by the two-step reaction of metal precursors. The project team was led by the Institute of Energy Conversion (IEC) at the University of Delaware partnering with Columbia University and the Molecular Foundry at the Lawrence Berkeley National Laboratory (LBNL).

IEC, with a unique H_2Se/H_2S reactor for research on this process, had previously characterized fundamental reaction pathways and formation kinetics. Based on these studies, the time-temperature reaction profile was used to control the Ga distribution through the film as shown in Figure 1 and to increase bandgap and V_{OC}[10]. IEC primarily uses precursors deposited by sputtering from $Cu_{0.75}Ga_{0.25}$ and In sputter targets – limited by materials properties that make fabrication of Cu-Ga sputter targets with higher Ga difficult. The precursors are reacted using a novel three-step $H_2Se/Ar/H_2S$ reaction process[11] that enables greater control of the relative Ga and S profiles and formation of large-grained films. SEM images of films after each step are shown in Figure 2. Step 1 is a reaction at ~400°C in H_2Se forming small grain films with a mixture of chalcopyrite and intermetallic (primarily Cu_9Ga_4) phases. An Ar anneal step at 500-600°C leads to recrystallization and Ga-In intermixing so the relative Ga profile is primarily controlled by the extent of reaction in the first step. Finally, a short 5-10 minute reaction step at 500 – 600°C in H_2S corrects for insufficient chalcogen and widens the near-surface bandgap[5]. Using this process with precursors containing Ga/(In+Ga) ≈ 0.25, IEC fabricated devices with highest-efficiency parameters V_{OC} = 630 mV and η = 15.0% for $Cu(InGa)(SeS)_2$ and $E_g \approx 1.15$ eV based on QE. Ag- alloying in the precursor reaction process has been shown to provide benefits including improved morphology and adhesion[12]. With a $(AgCu)(InGa)Se_2$ absorber layer reacted using a single step H_2Se reaction that results in backside Ga accumulation, a cell with V_{OC} = 515 mV, J_{SC} = 38.2 mA/cm^2, FF = 76.4%, and η = 15.2% was achieved.

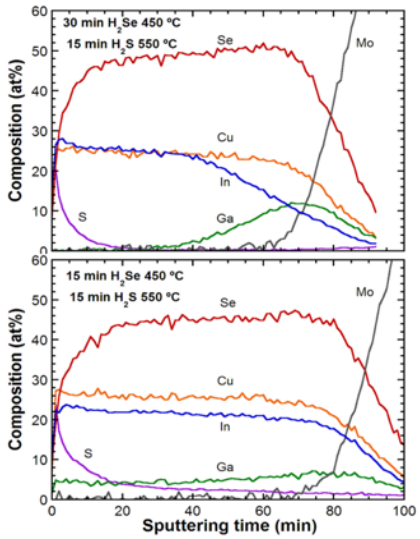

Figure 1. Composition depth profile of reacted films[10] (a) with Ga accumulation near back contact and (b) with Ga distributed through the film after modified reaction time-temperature profile.

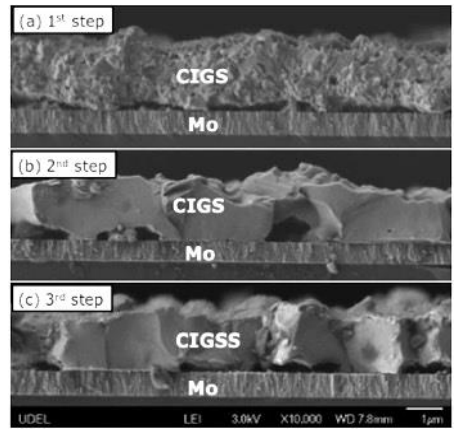

Figure 2. SEM images of films after each step of a three-step reaction process[11] showing void accumulation and increase in grain size. The CIGSS films are ~ 2 µm thick.

As of the start of this project, record cell efficiencies greater than 22% and modules greater than 16% have been demonstrated using the precursor reaction process. These efficiencies, while comparable to the best results using co-evaporation and other processes, have relatively lower open circuit voltages, attributed to the accumulation of Ga at the back contact and consequent low bandgaps, $E_g < 1.1$ eV.

This project proposed to develop pathways to improved performance of CIGSS modules using processes and materials compatible with low manufacturing cost. Approaches to improve the performance and specifically open circuit voltage of reacted films focused on increasing the overall Ga content to form reacted films with bandgap $E_g \geq 1.2$ eV, with the aim of demonstrating $V_{OC} \geq 720$ mV and efficiency $\eta \geq 18\%$ using commercially relevant soda lime glass substrates. This would require developing a process for deposition of high Ga precursor films using layer sequence and sputter parameters to control morphology and phase composition. Fundamental characterization of optoelectronic film properties and advanced device models will guide development of H_2Se/H_2S reaction processes to control relative Ga/In and S/Se profiles for reduced recombination. To overcome temperature constraints of soda lime glass, Ag-alloying was investigated since these materials are expected to have lower melting temperatures than Cu(InGa)(SeS)$_2$ alloys.

Main project objectives were to:

- Advance the technology for CIGSS using the reaction of metal precursors validated by demonstrating cell efficiency ≥ 18% with $V_{OC} \geq 720$ mV and a V_{OC} deficit $E_g/q\text{-}V_{OC} < 0.45$ V.
- Develop processes for precursor formation and controlled reaction using different film compositions with higher than ever gallium contents in the range 0.25 ≤

Ga/(In+Ga) ≤ 0.50.

- Investigate the advantages offered to selenized CIGSS films that result from alloying with silver, and demonstrate a proof of concept that will increase industry confidence in selenized ACIGSS devices.
- Demonstrate the benefits of newly developed selenization procedures and alkali post-treatments to the overall quality and performance of selenized CIGS materials.
- Gain fundamental understanding of the effects of material and process changes on local optoelectronic properties using high-resolution optoelectronic characterization based on two-photon TRPL.
- Transfer critical gains in precursor reaction technology to manufacturing by direct interaction with Stion and timely presentation and publication of key results.

The research project is best described in three overall technical area each encompassing multiple Tasks and Budget Periods. The focus and goals of each are described below.

I. Alloying and increased bandgap (Tasks 1 and 4; BP 1-2)

The composition of precursor and reacted films were modified with higher relative Ga content and Ag alloying to increase bandgap and V_{OC}. The focus was to develop a process to increase Ga/(In+Ga) to 0.5 and quantify the effects of higher Ga content on precursors and reacted films. The proposed approach was to procure a Cu_2Ga sputter target to enable higher Ga content than the Cu_3Ga target commonly used but the target vendor who promised this during the proposal stage reneged and no other vendors who would make such a target could be found. So higher Ga was achieved using an elemental Ga target along with the Cu_3Ga, Ag_3Ga and In targets. An additional research focus was on developing processes for incorporating Ag with higher Ga to increase V_{OC} by 100 mV. Finally this research area included and reacting and characterizing films and devices with the different precursor compositions to make a down-select for the preferred film composition based on device analysis and optoelectronic measurements of films.

II. Composition and surface control (Tasks 2, 5, and 7; BP 1-3)

The primary goal was to develop processes to control composition profiles by the reaction time-temperature profile with the goal of minimizing the recombination volume in the absorber layer for higher V_{OC} without losing optical absorption and J_{SC}. Advanced device characterization and modeling were utilized to understand the effects of relative Ga/In and S/Se gradients and their correlation to film and device results Expected results included, in Year 1, a comprehensive model for the bandgap profile of high efficiency cells using material and device parameters. In Year 2, processes were developed to control composition gradients in films with total Ga/(In+Ga) from 0.25 to 0.5 leading to increased V_{OC} and their effects on device behavior quantified. In Year 3, this research was intended to optimize composition, gradients, and alkali treatments leading to demonstration of cell efficiency ≥ 18% with V_{OC} ≥ 720 mV.

III. Materials characterization (Task 3, 6, and 8; BP 1-3)

Materials characterization performed primarily at LBNL focused on providing spatially resolved measurement of surface and bulk carrier lifetime as well as other optoelectronic

properties to provide new understanding of reacted films from IEC and Stion and to guide optimization of Ga content, Ag-alloying, composition gradients, and surface treatments. Expected results in Year 1 included development of a new tool and procedure for two-photon (2P) TRPL measurements in the near-IR range and characterization of CIGSS devices. In Year 2 lifetime measurements were to be correlated with depth in graded CIGSS films to create 3D maps of lifetime in thin-film CIGSS cells and films with different compositions and gradients will be fully characterized. In Year 3, combined photocurrent and lifetime mapping of CIGSS cells would allow for characterization of the microscopic origins of optoelectronic performance changes with precursor ratios as well as with metastability changes.

There were three significant adjustments to the project during its progression:

1. Stion Corporation was part of the initial project team with several roles. These included (a) providing materials and devices for comparison to materials developed at IEC, (b) providing guidance as to the relevance of the research and its feasibility for manufacturing relevance, and (3) providing a potential pathway for transfer of critical gains in precursor reaction technology to manufacturing. During the second Budget Period, Stion went out of business so these interactions ceased.
2. During the third Budget Period, the baseline process being developed was changed. Previous work focused on a long, batch reaction of metal precursors as used in manufacturing by Stion. In discussion with the SETO program managers, the primary process focus changed to a faster reaction using a Rapid Thermal Process (RTP) heating capability on the IEC H_2Se/H_2S reactor. This refocus was taken on in lieu of further process optimization with the long reaction. A consequence was that the final project milestones, as discussed below, were not achieved.
3. A budget revision and six month No-Cost Extension were applied to the project. This changed the end date from 8/31/2019 to 2/29/2020.

Project Results and Discussion

I. Alloying and increased bandgap

Cu-In-Ga Precursors

Precursors were prepared using a DC sputter system equipped with Mo, Cu_3Ga, Cu, In, and Ga targets. Two sets of precursors were prepared for this work, an elemental stack using the Cu, In, and Ga targets, and an alloyed stack, which replaced the Cu target with Cu_3Ga. The elemental stack followed the sputtering order Cu/Ga/In, whereas the alloyed stack used Cu_3Ga/In/Ga. All precursors were deposited to a thickness of 500-700nm onto Mo coated soda-lime glass.

Figure 3(a) shows SEM plan-view images of as-deposited Cu/Ga/In precursor stacks with Ga/(In+Ga) ≈ 0.00, 0.25, 0.50 and 0.75. An as-deposited co-sputtered Cu-Ga/ In precursors with Ga/(In+Ga) = 0.25 and $Cu_{0.75}Ga_{0.25}$/Ga/In precursor stacks with Ga/(In+Ga) = 0.35, and 0.5, and a Stion precursor are shown in Figure 3(b). Regardless of as-deposited precursor sequence, x-ray diffraction (XRD) analysis of films with Ga/(In+Ga) = 0.25 and 0.50 Ga films annealed at 300ºC indicated only In, $Cu_9(InGa)_4$,

and $Cu_{16}(InGa)_9$ phases. However, in these samples, the use of elemental Cu and Ga targets induces finer-grained surface agglomerates which contain the In. Segregation in the $Cu_{0.75}Ga_{0.25}$/Ga/In precursors appears to be worse with increasing Ga content and the effect of this on the reaction process and device performance will be assessed. Modification of the sputter parameters was investigated to form denser films.

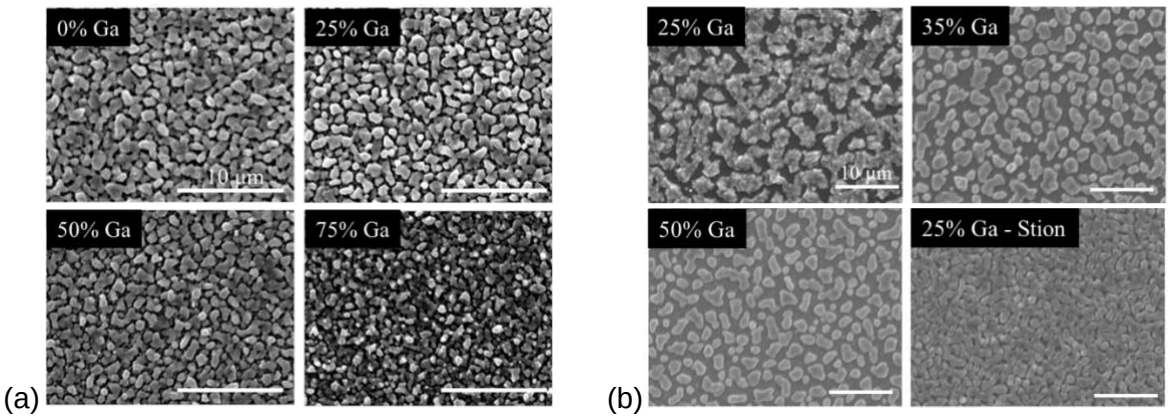

Figure 3. (a) SEM plan-view images of as-deposited Cu / Ga / In precursor stacks with Ga/(In+Ga) ≈ 0.00, 0.25, 0.50 and 0.75 and (b) as-deposited $Cu_{0.75}Ga_{0.25}$/Ga/In precursor stacks with Ga/(In+Ga) = 0.25, 0.35, and 0.50. A Stion precursor is shown for comparison.

Precursors were annealed in Ar to characterize phase evolution with temperature and measured using X-ray diffraction (XRD). The alloyed samples were annealed for 1 day in flowing Ar at various temperatures up to 300°C, whereas the elemental samples were annealed up to 450°C in an in-situ XRD apparatus.

Morphology was characterized using SEM for precursors with varying Ga ratio from $x = 0.25 - 0.75$ that were deposited with the alloyed stack method. Figure 4 shows plan-view SEM for the different Ga composition precursors. Precursors deposited using our sequential sputtering approach consistently show surface agglomerations which are composed primarily of In, and form during the In sputtering process. Individual In grains on the precursor surface were quantified using a greyscale thresholding automated approach. The grain area density (ρ, percentage of surface that is covered by In agglomerations), median grain size, and average grain size are shown in Figure 4.

Comparing coverage and median grain sizes, there is no consistent effect on morphology from changing the amount of Ga sputtered. It is likely that the primary contributing factor in this test case is the amount of In that is sputtered. As the Ga ratio is increased, the total In sputter time is decreased to allow for the inclusion of more Ga, which results in a change in morphology. Starting at $x = 0.75$, it is observed that a large amount of small In agglomerations form, although they remain mostly spatially separated. For the $x = 0.50$ case a similar phenotype is observed, although the size of the grains is increased which causes some to form together into larger agglomerations. For both of the lower Ga concentrations, the grain morphology is characterized by many smaller grains that fill in the void space between larger agglomerations. These two films both have more inconsistently sized agglomerations, which is possibly due to more In nucleation events occurring over the longer sputter time in these cases, causing more smaller grains to form later in the process. Between the two however, the $x = 0.25$ case has increased

agglomeration size, which is also consistent with additional In sputtering time causing more growth of the existing grains.

Although it is still unclear if the film surface morphology has a noticeable effect of device performance, it is hypothesized that a more uniform precursor morphology would aid in a uniform reaction process downstream. To this end, the $x = 0.50$ precursor appears to yield the best morphology, with high surface coverage and large agglomeration size.

It was hypothesized that the density of the In features that form on the precursor surface is proportional to the impact energy of sputtered In particles, where higher energy particles are more likely to cause a new nucleation event on the deposited surface. The two primary methods of increasing the agglomeration density are substrate cooling – which reduces movement of In particles after they strike the film increasing the In impact energy to cause increased agglomeration nucleation. Additionally, it was verified that after annealing the precursors, the film morphology did not change, although, the composition of Cu and Ga in the agglomerations increased. The change in composition of the agglomerations post-annealing suggests that there may be an effect on the reaction process or final reacted film morphology based on the precursor morphology.

Because active substrate cooling is not acheivable in all sputter systems, the effect of In impact energy was investigated. The two primary controls during the sputtering process are the sputter power, and the chamber deposition pressure. By increasing sputter power, In particle energy is also increased proportionally, however, the impact energy is also controlled by the deposition pressure. When pressure is increased, sputtered In particles will experience more collision events before striking the substrate surface, thus impact energy is inversely proportionate to deposition pressure.

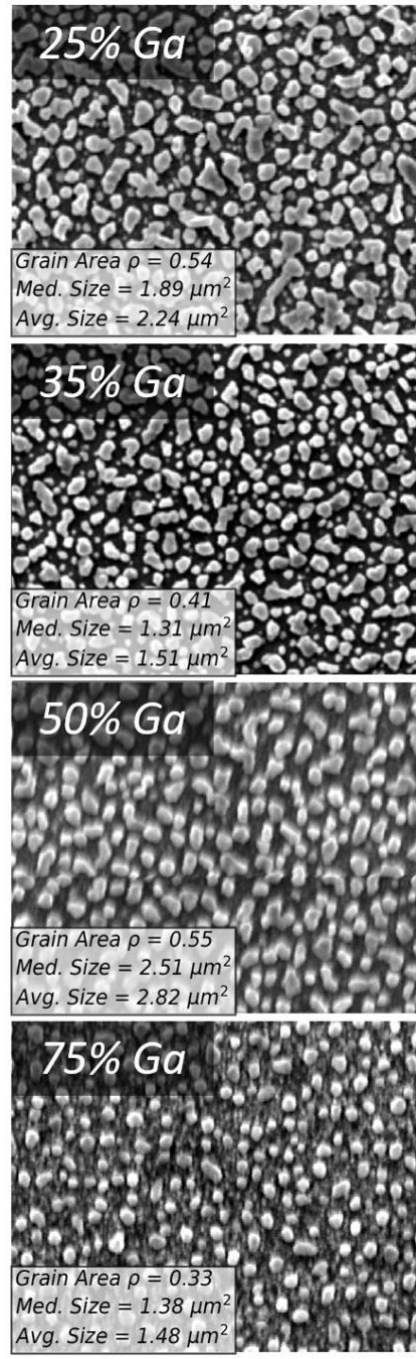

Figure 4. Film morphology for films with various Ga compositions ranging from $x = 0.25$ - 0.75.

To verify that precursor morphology can be controlled using this method, Cu-In-Ga precursors were sputtered at various conditions with sputter power ranging between 100W220W, and deposition pressure ranging from 5mTorr-20mTorr. Plan-view SEM in Figure 5 shows how precursor morphology changes with sputter condition. It is observed that the grain area density (ρ) decreases for increasing deposition pressure, and size, the trend is less clear, with most sputter conditions resulting in similar median size. This

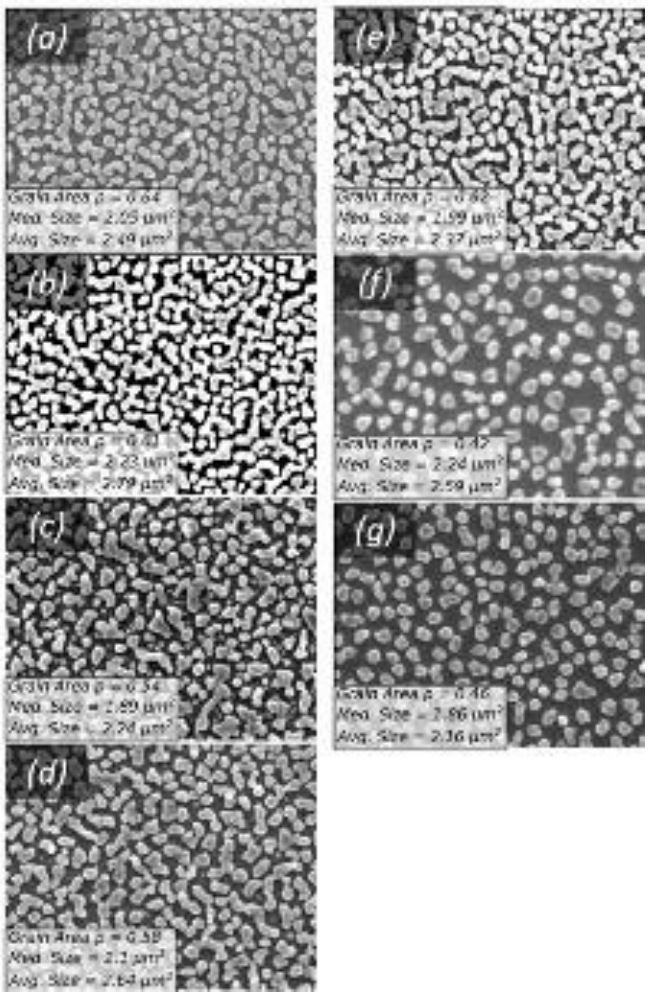

Figure 5. Film morphology for films with In sputter conditions of (a) 5mTorr 140W (b) 5mTorr 220W (c) 10mTorr 100W (d) 10mTorr 140W (e) 10mTorr 220W (f) 20mTorr 100W (g) 20mTorr 140W.

implies that the agglomeration growth once formed may be fixed by additional factors and changing these sputter conditions only serves to change the density of their formation.increases for increasing sputter power. This results in the highest grain area ρ at 220W/5mTorr, and 220W/10mTorr conditions. Comparing median agglomeration

Using the alloyed sputtering stack, precursors with x = 0.25, 0.35, and 0.50 were deposited and annealed at 100, 200, and 300°C. XRD patterns for the various samples are shown in Figure 6. For the as-deposited films at all compositions, the In and Cu_3Ga phases are observed. Additionally, $CuGa_2$ is observed for both of the increased Ga precursors. For the x = 0.25 case, however, $CuGa_2$ is not present and instead $CuIn_2$ is observed. After annealing at 100°C, the $CuGa_2$ is replaced by $Cu_9(In,Ga)_4$ for the x = 0.35 and 0.50 samples. This is also observed for x = 0.25, although $CuIn_2$ is still present at 100°C. Comparing between the three Ga compositions, the $Cu_9(In,Ga)_4$ peak is shifted to higher angle with higher Ga ratio. This is because the ratio of Ga to In in the $Cu_9(In,Ga)_4$ is increased for the higher Ga films. In the case of the x = 0.25 precursor, the $Cu_9(In,Ga)_4$ consists of primarily In.

Increasing the temperature up to 200°C results in increased intensity of $Cu_9(In,Ga)_4$ for all samples, additionally Cu_3Ga is no longer observed at this temperature. In the x = 0.25 sample the Cu_2In phase replaces the Cu_3Ga. As phase evolution progresses with the anneal, the as-deposited phases become incorporated into precursor phases. Due to the high ratio of In present in the x = 0.25 sample, after 200°C In becomes incorporated into the Cu_2In phase instead of the $Cu_9(In,Ga)_4$. This is consistent with the $Cu_9(In,Ga)_4$ peak position shifting to higher angle from 100°C to 200°C, which indicates that less In is being incorporated into this phase and it is becoming Ga rich. For the x = 0.35 and 0.50 films, the $Cu_9(In,Ga)_4$ peak position decreases as more In is incorporated. When x =0.35 the Cu_2 phase is still observed, but at reduced intensity compared to x =0.25. Increasing the Ga to x = 0.50 results in the Cu_2In phase no longer being observed, with only a $Cu_9(In,Ga)_4$ phase that incorporates both the In and Ga.

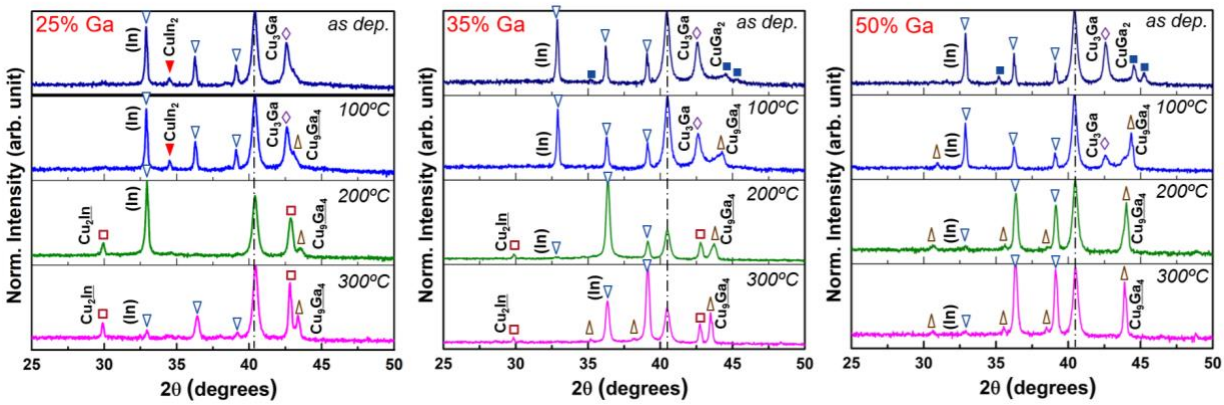

Figure 6. XRD patterns for as deposited and various anneal temperatures for x = 0.25, 0.35, 0.50

After annealing at 300°C, generally the same phases are observed as for 200°C, although the intensity of the final precursor phases, such as Cu_2In and $Cu_9(In,Ga)_4$ are increased across the board as remaining Ga and In is incorporated. At this point, the only remaining as-deposited phase is elemental In, which is observed in all Ga ratio samples. However, the peak intensity tends to decrease as Ga ratio increases, implying that less In is incorporated into the precursor phases at higher Ga. Additionally, the presence of both Cu_2In and $Cu_9(In,Ga)_4$ phases for $x = 0.25$ and 0.35 indicates that separate In and Ga rich precursor phases are being formed, which tend to remain as separate phases. In contrast, when the Ga is increased to $x = 0.50$, only the $Cu_9(In,Ga)_4$ is observed, indicating both Ga and In being incorporated into a single mixed phase, however, this also coincides with an apparent decrease in In uptake at high Ga.

Progress toward wide bandgap, Ag-bearing precursors proceeded by first independently examining the effects of higher Ga content and Ag incorporation into baseline precursors. The incorporation of Ag into precursors with 25% Ga has previously been thoroughly characterized for the effect of sputtering sequence on morphology and for compositional stability using the sequence Mo/Cu-Ga/In/Ag-Ga which gave the highest device efficiency.[13] A comprehensive analysis of phases and morphology in these precursors was completed in this project.[14,15] A key finding was that the phases were not stable over time in storage so the evolution and distribution of intermetallic phases during annealing in Ar was quantified. Figure 7 shows the phase evolution with annealing in a precursor with Ag/(Cu+Ag) = 0.25. After annealing, the films contain $(Ag_{0.72}Cu_{0.28})In_2$, Cu_9Ga_4, $Cu_{0.18}In$ and Cu_3Ga with increasing Cu in the $(Ag_{1-x}Cu_x)In_2$ phase, reduction of the In phase and segregation of Ga toward the back of film. Further annealing did not change these films so the starting point for reaction is stable.

A unique outcome of the precursor studies completed in this project was the discovery of a new quaternary Laves-type phase in sputter-deposited and evaporated thin films of Ag-Cu-In-Ga (ACIG) and publication of its x-ray diffraction pattern[15]. The corresponding powder diffraction file has been added to the International Centre for Diffraction Data (ICDD) database. Films with different compositions were analyzed by energy dispersive x-ray spectroscopy and x-ray diffraction to determine composition and structure based on Rietveld whole pattern refinement. Annealing and partial reaction with H_2Se were used to

study the phase. The quaternary phase corresponds to $(Cu_{1-x}Ga_x)_2(Ag_yIn_{1-y})$ with x ≈ 0.2 and y ≈ 0.3. It has a Cu_2Mg-type crystal structure with space group of Fd3m and lattice parameter of 7.090. Specifically, formation of this phase was reported in the composition range (Ag + Cu)/(In + Ga) ≈ 0.8–0.9 suitable for precursors to the formation ACIGS solar cells.

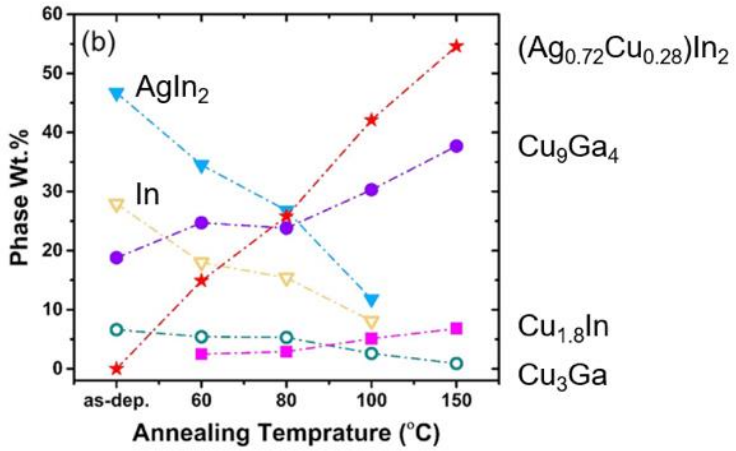

Figure 7. Phase progression with increasing annealing temperatures for Mo/Cu-Ga/In/Ag-Ga precursors.

Precursors deposited and characterized as described above were subsequently used in reaction studies. In particular, a study[16] of formation of $(Cu_{0.75}Ag_{0.25})(In_{0.75}Ga_{0.25})Se_2$ was extended to determine reaction pathways during formation of ACIGS films with Ag/(Cu+Ag) = 0, 0.25, 0.75, and 1.0, with Ga/(In+Ga) = 0.25. This was investigated by ex-situ characterization of time-progressive reactions using rapid thermal processing at 450°C under a 5% Ar/H2Se atmosphere. Composition measurements using energy dispersive x-ray spectroscopy (EDS) and X-ray fluorescence (XRF) show that with Ag/(Ag+Cu) = 1.0, Ga grading and Se uptake occur gradually up to 20 min. With 7 min reaction, there was no sign of a $AgInSe_2$ phase and only a $Ag(In,Ga)_5Se_8$ chalcogenide phase formed. The reaction was completed with formation of $Ag(In,Ga)Se_2$ and $Ag(In,Ga)_5Se_8$ within 20 min. The addition of Cu to the precursor so that Ag/(Ag+Cu) = 0.75 speeds up the reaction and reduces the formation of the $Ag(In,Ga)_5Se_8$ phase. EDS and XRF analyses indicated that Ga grading and Se uptake were completed after 10 min. A critical result from the complete study is the determination that a mixture of Ag and Cu increases the reaction rate at 450°C so that the complete reaction to chalcopyrite is faster as shown in Figure 8. In all cases, $Cu_9(In,Ga)_4$ is the slowest reacting phase, but in the Ag-alloys this is consumed in 10 min while it persists for 16 min in the reaction of pure Cu-Ga-In under these conditions.

Baseline reaction and device fabrication

For fabrication of CIGSS absorber layers a soda lime glass substrate is coated with ~ 0.6 µm thick Mo deposited by dc sputtering. Metal precursor layers Cu-Ga-In or Ag-Cu-Ga-In are deposited after the Mo in the same sputter system, in most cases without breaking vacuum. The precursor films were reacted in the IEC H_2Se/H_2S reactor's 2" diameter quartz tube with heating jacket which enables temperature up to 600°C and a push-pull

rod that enables samples to be inserted or removed from the hot reaction zone. Before reaction, the reactor was evacuated to 5 x10^{-6} Torr to remove moisture and impurities. Then, Ar gas was introduced in the reactor and the pressure was allowed to reach one atmosphere. Ar flow was maintained through the entire reaction with a nominal turnover time of about 1 min. Reactions were done in in flowing H_2Se(0.35%) / Ar(balance) or flowing H_2S(0.35%) / Ar(balance). The baseline process starts with reaction at 400 – 450°C in H_2Se which forms a small grain film containing a mixture of chalcopyrite and intermetallic (primarily Cu_9Ga_4) phases. This is followed by an anneal step at 500-600°C which leads to significant recrystallization and Ga-In intermixing so the relative Ga profile is primarily controlled by the extent of reaction in the first step. Finally, a short 5-10 minute reaction at 500 – 600°C in H_2S doesn't change the morphology but corrects for insufficient chalcogen and widens the near-surface bandgap[5].

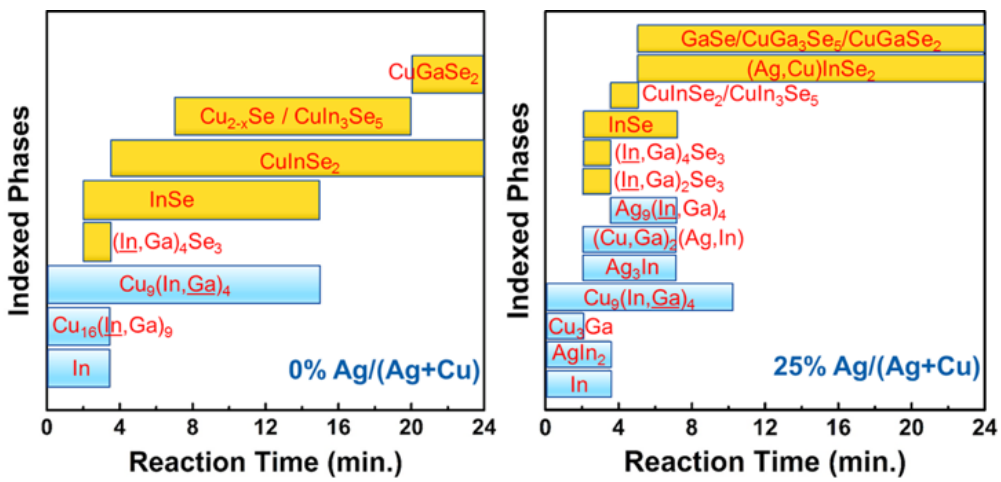

Figure 8. Phase evolution during precursor reaction in H_2Se at 450°C to form CIGS (left) and ACIGS (right). ACIGS reaction is completed in 10 min.

In this project, three reactor upgrades were implemented. First, a new turbopump system was purchased and installed. Second, an improved hydride gas scrubber was installed. Third, the reactor temperature control scheme was identified as a source of irreproducibility so an improved temperature measurement and control scheme was developed and implemented.

Devices have been fabricated with a conventional Mo/CIGSS/CdS/i-ZnO/ITO/Ni-Al structure. A 50 nm thick CdS layer was deposited on the CIGSS absorber layer by chemical bath deposition (CBD) and i-ZnO (50 nm)/ITO (150 nm) layers with sheet resistance 30 Ω/sq were deposited by RF magnetron sputtering. Finally, grids of Ni (50 nm)/Al (3000 nm) were deposited by e-beam evaporation. Cells were delineated by mechanical scribing with area 0.4 or 1.0 cm^2.

Initial experiments to develop a multi-step H_2Se/H_2S reaction time-temperature profile to control through-film composition were carried out using the baseline reaction described above and illustrated in Figure 10(a)[11]. Figure 10(b) shows SEM plan-view and EDS/XRF analysis of IEC co-sputtered and Stion precursors. After reaction, these films had Ga/(In+Ga) ≈ 0.14 and 0.45, respectively measured by EDS which samples the top ~ 0.5

µm of the film. The XRD values show the composition ratios averaged over the entire film thickness. The difference indicates increased Ga homogenization compared to a single-step reaction. We do not have an explanation for the excess Ga and Se on the top of the Stion precursor.

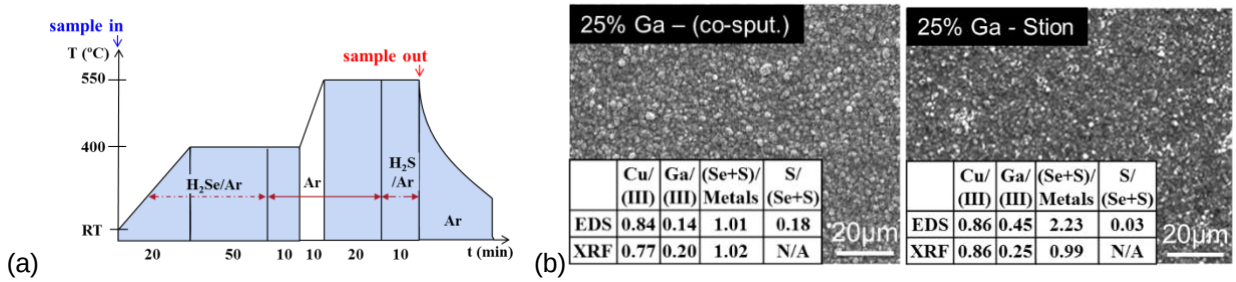

	Cu/ (III)	Ga/ (III)	(Se+S)/ Metals	S/ (Se+S)
EDS	0.84	0.14	1.01	0.18
XRF	0.77	0.20	1.02	N/A

	Cu/ (III)	Ga/ (III)	(Se+S)/ Metals	S/ (Se+S)
EDS	0.86	0.45	2.23	0.03
XRF	0.86	0.25	0.99	N/A

Figure 10. (a) Schematic of three-step reaction and, (b) SEM plan-view images of the reacted co-sputtered precursor. EDS/XRF analysis are also shown.

Figure 9 and Table 1 show JV curves and their related parameters of baseline cells using IEC and Stion precursors with Ga/(In+Ga) ≈ 0.25 with the multi-step reaction. The IEC co-sputtered reacted sample had initial Eff. = 13.1% with V_{OC} = 539 mV. The cell was then annealed at 200ºC for 2 min in air and its performance improved to give Eff. = 13.9% with V_{OC} = 570 mV. Comparable efficiency with higher V_{OC} = 594 mV was obtained in the initial test using the Stion precursor cell. It must be noted that the Stion precursor contains controlled Na while with the IEC precursor Na is supplied by diffusion from the SLG.

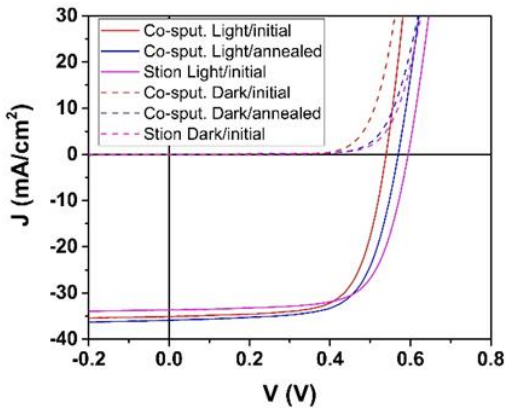

Figure 9. Initial and annealed JV curves under illumination and in the dark of the multi-step reacted co-sputtered precursors.

Table 1. J-V parameters of the multi-step reacted co-sputtered precursors.

Precursor	Test condition	V_{OC} (mV)	J_{SC} (mA/cm^2)	FF (%)	Eff. (%)
IEC	Initial	539	35.1	69.0	13.1
IEC	Annealed	570	35.9	67.8	13.9
Stion	Initial	594	33.7	69.4	13.9

In an informative set of experiments, Cu-In-Ga films with Ga/(In+Ga) = 0.25 were reacted using a range of H_2Se/H_2S or $H_2Se/Ar/H_2S$ process variations building on previous studies. A key result quantified the dependence of the extent of reaction, controlled by time and temperature, in the first H_2Se reaction step on the later S incorporation. For example, reaction in H_2Se for 70 or 120 min at 400°C followed by Ar anneal and H_2S reactions of 10 min at 550°C resulted in surface S concentration of S/(Se+S) = 0.5 or 0.1 respectively. The resulting conduction band barrier with high S creates a voltage-dependent collection which results in devices with significantly reduced FF, as shown in

Figure 11, even though V_{OC} is not affected. Reaction in H_2Se for 90 or 120 minutes was established as a reproducible baseline process, with efficiency ≥ 15% over 3 consecutive runs, and starting point for investigations of both higher Ga content and Ag incorporation.

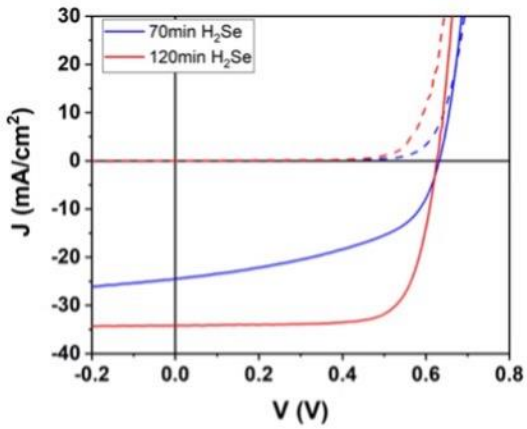

Figure 11. JV curves for devices with H_2Se reaction for 70 or 120 min then 10 min Ar anneal and 10 min H_2S reaction at 550ºC.

Device results with either higher Ga or Ag incorporation did not initially achieve the performance of the baseline process. Cu_3Ga/In/Ga precursors with 0.25 ≤ Ga/(In+Ga) ≤ 0.5 were deposited and fully characterized with respect to phase composition and morphology as described above. Table 2 compares the compositions of baseline and 50% Ga precursors after three-stage H_2Se/Ar/H_2S reaction processes with varying H_2Se reaction times. At 10 or 90 min reaction, the baseline Ga/(In+Ga) =0.25 precursors give S/(Se+S) ratios < 0.10, as measured by EDS. In contrast, the Ga/(In+Ga) =0.5 Ga precursors yield 0.24 < S/(Se+S) < 0.43 across the same range of reaction times. This result is consistent with previously known slow Ga selenization kinetics resulting in a higher quantity of unreacted metals available for sulfization during stage 3. As a result, devices produced using higher Ga content have current blocking behavior that leads to low J_{SC} and FF. Thus, a wider range of reaction conditions, including increased selenization temperatures were studied. Interestingly, reacted films exhibited good adhesion up to 475C, whereas baseline precursors typically exhibit adhesion issues below 450°C.

In this task area, processes were developed to deposit Cu-Ga-In and Ag-Cu-Ga-In precursors from Cu_3Ga, Ag_3Ga, Ga and In sputter targets. Precursor films with Ga/(In+Ga) = 0.5 were compared to typical precursors with Ga/(In+Ga) = 0.25 and shown to have comparable phase composition and morphology. This indicates that reaction of higher Ga films will follow from the same starting point as the well-studied lower Ga case. A baseline process to form CIGSS was established to give reproducible efficiency from 15-16% without AR layers.

Phases in Ag-containing precursors with Ga/(In+Ga) = 0.25 were determined over the complete composition range from 0 ≤ Ag/Cu+Ag) ≤ 1. Time variation in the precursor phase composition was also characterized and stability after annealing in Ar, analogous to the beginning of any reaction process, was demonstrated. A significant result was the determination that Ag-alloying increases the reaction rate to completely convert intermetallic precursor films to chalcopyrite during reaction at 450°C. With all precursors, $Cu_9(In,Ga)_4$ is the slowest reacting phase but in alloys containing both Ag and Cu, this is completely consumed in 10 min while it persists for > 16 min in the reaction of pure Cu-Ga-In or Ag-Ga-In under these controlled conditions.

Development of reaction processes to control through-film and surface composition in order to control device behavior is the focus of Tasks 2,5, and 7 as described below.

Table 2. Sulfur uptake in precursors with Ga/(In+Ga) = 0.5, reacted using a three-stage H_2Se, Ar, H_2S process for varying H_2Se reaction times.

EDS	H_2Se reaction time (min)		
	120	90	70
Cu/(In+Ga)	0.92	0.94	0.95
Ga/(In+Ga)	0.19	0.21	0.20
(S+Se)/Metal	0.97	0.99	0.98
S/(S+Se)	0.03	0.09	0.25
Cu/(In+Ga)	0.99	1.03	1.05
Ga/(In+Ga)	0.43	0.40	0.43
(S+Se)/Metal	1.03	1.01	0.99
S/(S+Se)	0.24	0.34	0.43

II. Composition and surface control

Composition profiles are controlled by the reaction time-temperature profile with the goal of minimizing the recombination volume in the absorber layer for higher V_{OC} without losing optical absorption and J_{SC}. Relating the composition and through-film bandgap profiles to correlate reacted film characteristics to device performance is guided by models of device behavior.

Device Modeling and Characterization

Device characterization and modeling were used to understand and the role of gradients in the CIGSS devices. Using a similar methodology as in previous work[17], admittance spectroscopy (AS), drive level capacitance profiling (DLCP), V_{OC} – T, and secondary ion mass-spectrometry (SIMS) composition depth profiles were used to build a model of the CIGSS solar cell. SIMS profiles and device characterization input from devices with different selenization times and sulfur gradients are input into the SCAPS numerical simulation program[18] without changing the basic fitting parameters. If a good fit can be obtained without altering the model, it shows that the E_g gradients and defect/doping densities are enough to explain changes in device behavior. If we find the model robust, then an optimized profile can be discovered by using the model as an optimization tool. Otherwise, the model can be used to explain efficiency limitations in the devices. In addition to the numerical modeling, we have found differences in AS spectroscopy in forward bias in low sulfur and high sulfur samples. This indicates the presence of additional defects in the sulfur surface layer that may limit the amount of useful sulfur alloying by limiting V_{OC} and FF.

For the SCAPS simulation, in order to describe sulfur and gallium gradients, the CIGSSe absorber layer was divided into two slabs, a front region with fixed Ga/(In+Ga) and changing S/(Se+S), and a back region with fixed S/(Se+S) and changing Ga/(In+Ga). This simplification is used due to limitations within the SCAPS software, but describes the measured compositional gradients well[17]. Acceptor concentrations (N_A), measurable defect densities (N_t), defect energies (E_t), and capture cross sections (σ_t) were obtained from DLCP and AS measurements, and input into the SCAPS model. Finally, a deep defect positioned at 0.8eV + E_V was used as a fitting parameter. All devices have comparable V_{OC}, while devices with increased S/(S+Se) show lower FF mostly due to

voltage dependent photo collection(Table 3). Diode analysis[19] shows similar series resistance and dark shunt resistance.

Table 3. JV parameters and composition from EDS measurement for devices used in simulations.

Stage 1 Reaction	V_{OC} (mV)	J_{SC} (mA/cm^2)	FF (%)	S/VI	Ga/III	E_g(eV) (EDS)
70 min	607	24.8	51.7	25	20	1.26
85 min	596	30.7	64.8	16	20	1.21
90 min	616	32.6	72.2	9	21	1.17

DLCP was measured over a temperature range of 100K to 300K at 100 kHz in order to ensure any AS step was traversed by the DL measurement. A profile of responding charge (N_{DL}) vs moment of charge response (<x>) was generated from the DLCP measurements. In addition to DLCP, Miller C-V profiles were calculated from C-V curves at 100K and 300K at the same frequency. Since these N_{CV}(<x>) profiles are distorted by interface and deep defects[20] differences between the CV and DLCP N_x(<x>) profiles can be attributed to either interface states or deep defects. Figure 12(a) shows a large difference between the N_{CV} and N_{DL} in the 70 minute device, with N_{DL} approaching N_{CV} at forward bias (small <x>). N_{DL} at 300K represents free carrier response in addition to deep defects, and seems to increase as <x> decreases. This seems to indicate an increased defect density in the sulfur rich region. Figure 12(b) shows good agreement between N_{DL} and N_{CV} for 90 minute device, indicating an absence of trap states or interface states that can cause a C-V profile to overestimate responding charge.

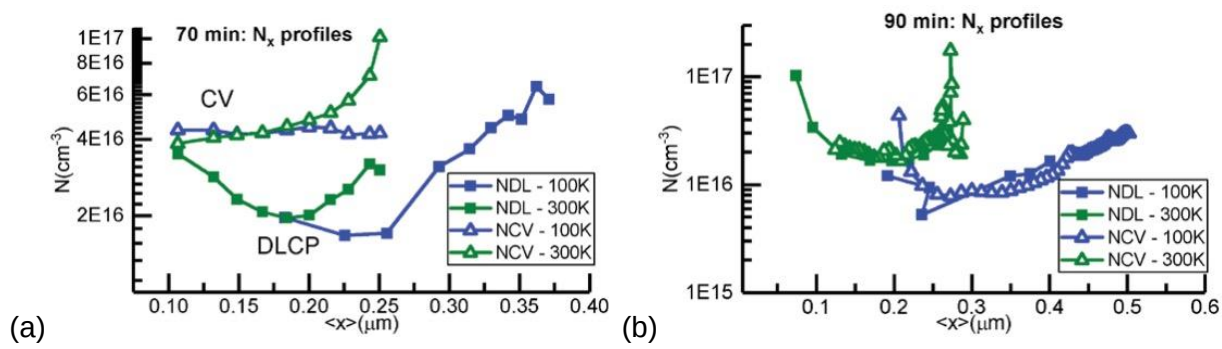

Figure 12. NCV,DL(<x>) for (a) 70 minute device and (b) 90 minute device. DLCP (closed symbols) and CV (open symbols) data are shown at at 100K (blue) and 300K (green).

AS curves were measured at 0V DC from 100K to 300K and the resulting densities of states (DoS) showed no evidence of states beyond 70meV Both samples exhibited a shallow step that could be observed from 100K to ~140K. At forward bias

SIMS compositional depth profiles were measured by Evans Analytics Group. Ga/(In+Ga) and S/(S+Se) depth profiles were calculated from the SIMS measurements shown in Figure 13. These were used to calculate E_g depth profiles were calculated for all devices using the empirical equation from Bär[21]. For numerical simulation, simplified E_g profiles were represented by three regions, R1, R2, and R3, with thicknesses x1,x2, and x3. Thickness x1 was set where the front Ga/(In+Ga) stops, x2 at the position where the

S/(S+Se) gradient stops, and x3 at the back contact. E_g and electron affinity (χ_e) were calculated at each region and assumed to vary linearly. E_g changes due to Ga alloying were assumed to proportionally decrease χ_e and E_g changes from S alloying were assumed to decrease χ_e by ½ of the E_g change.

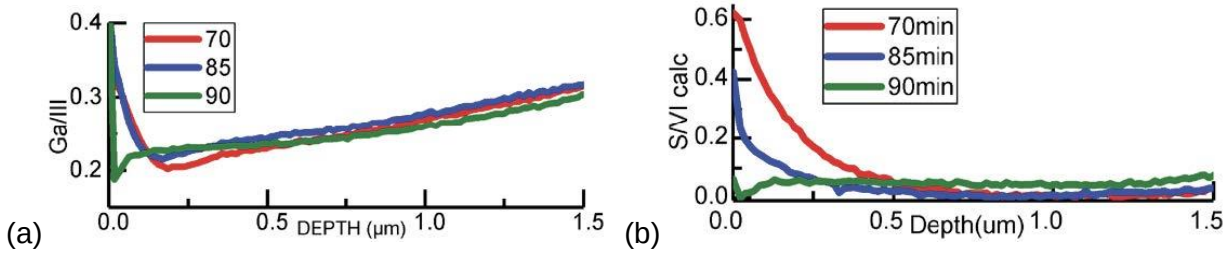

Figure 13. Composition depth profiles from SIMS measurements (a) Ga/(In+Ga) and (b) S/(S+Se).

A model was created for each device based on measured bandgap profiles, and C-V measurements to set hole concentration in the absorber layer. Based on the initial models, simulation over-estimated V_{OC}, FF, and efficiency. Since the 90 min sample had no sulfur gradient, it was used for curve-fitting purposes to establish parameters for a recombination center. A neutral mid-gap defect with initial electron and hole capture cross sections (σ_e, σ_h) of 1E-12 cm^2. The SCAPS curve fitting function was used to allow the trap density (N_t), σ_e, σ_h to vary freely to obtain a good fit for the light and dark JV curves, (Figure 14) and dark QE curve (not shown). The same defect was added to the models for the 70 and 85 min devices, but there was still poor agreement between the simulated and measured JV curves. In order to achieve good agreement between the measured and simulated JV, N_t was allowed to vary freely for each layer, while σ_e and σ_h were fixed. Good agreement was found for all three devices. Figure 15 shows N_t for each layer (R1,R2,R3) from all models vs the average S/(S+Se) from that region.

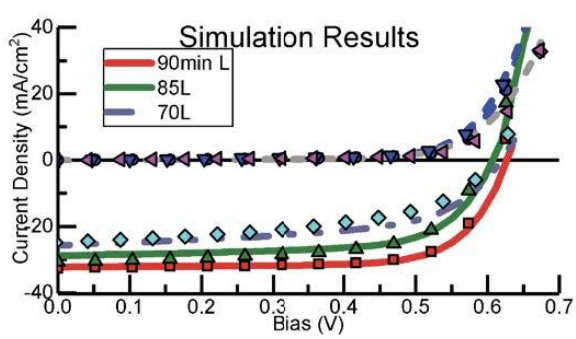

Figure 14. Simulated JV curves from SCAPS(symbols) and measured JV curves (solid).

The simulations suggest increased deep defects or interface defects with increased sulfur incorporation, evidenced by $N_{CV} > N_{DL}$. There is evidence of an additional defect at 100meV + E_V from AS with forward-biased high sulfur devices. Plotting N_t from SCAPS curve fitting vs the average S/(S+Se) in each layer, we see a exponential relationship between S/(S+Se) content and N_t (Figure 15). High sulfur incorporation can reduce FF due to voltage dependent photo-current collection. This is due to a reduction in electric

field strength in the space-charge region, as S/(Se+S) alloying increases E_c. Our SCAPS modeling suggests that this FF loss can be mitigated by higher minority carrier lifetime. It is the combination of reduced field and reduced diffusion length that causes increased minority carrier recombination.

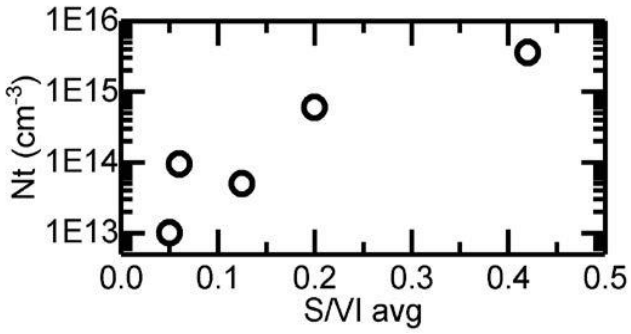

Figure 15. Trap state density from SCAPS fitting vs average S/(S+Se).

Composition gradient control

A research focus was on the control of composition profiles by the reaction time-temperature profile to minimize the recombination volume in the absorber layer for higher V_{OC} without losing optical absorption and J_{SC}. A set of CIGSS films were formed by the 3-step $H_2Se/Ar/H_2S$ reaction process of Cu-In-Ga precursors with Ga/(In+Ga) = 0.25 and varying the H_2Se reaction time from 10 to 120 min. SIMS composition depth profiles are shown in Figure 16. Surprisingly, the only significant difference is the S-profile in the near surface region. The relative Ga distribution is similar for all films.

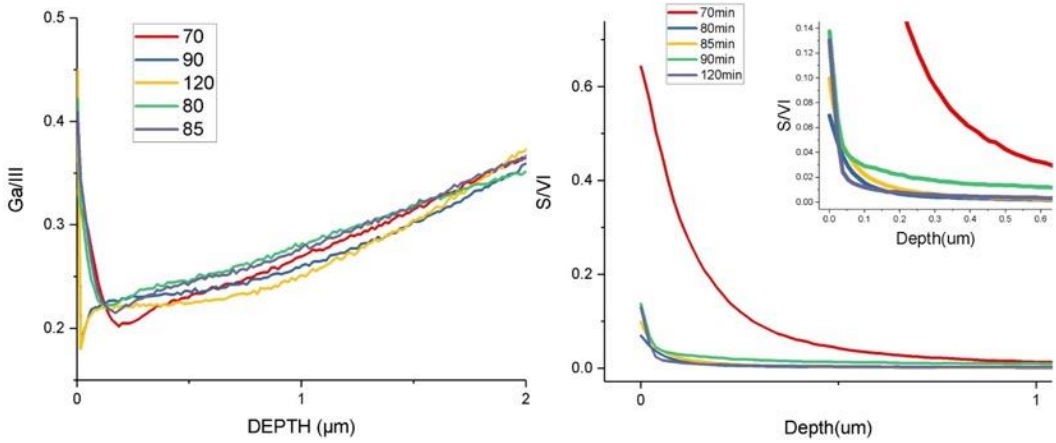

Figure 16. Composition depth profiles over entire film (left) and detail near the front surface (right) of CIGSS films formed by 3-stage reaction of precursors with the H_2S reaction time varied from 10 to 120 minutes.

Precursors with Ga/(In+Ga) = 0.5 were also processed by three-stage reaction with H_2Se reaction times of 70, 90, and 120 minutes at 400ºC. These all yielded absorbers with equivalent front- and back-side compositions Ga/(In+Ga) = 0.45. The high degree of homogenization observed in the three-stage process is consistent with a high content of unreacted, highly mobile metals at the end of the H_2Se reaction. With respect to S content, the 70- and 90-min selenized films had S/(Se+S) = 0.32 at the frontside and S/(S+Se) =

0.19 at the backside, while the 120-min selenized sample exhibited frontside S/(S+Se) = 0.19 and backside S/(S+Se) = 0.16. This variation in S profiles is not understood.

Characterization and modeling of $Cu(In,Ga)(Se,S)_2$ based solar cell devices with different gradients has shown that the front sulfur compositional gradient controlled by varying the selenization time is a critical variable in determining device behavior. Detailed device characterization, including admittance spectroscopy (AS), drive-level capacitance profiling (DLCP), and open-circuit voltage vs temperature (V_{OC}-T) measurements, as well as atomic-composition-depth profiles were input into numerical simulations to find an optimized front E_g gradient. In addition, we found that forward biased AS shows an additional defect in the sulfur rich layer of the device. Numerical simulation indicates conduction band barriers due to sulfur gradient in the presence of minority carrier traps can reduce minority carrier collection by reducing the field strength in the space charge region, resulting in increased voltage dependent collection (Figure 17). Actual devices show lower than expected V_{OC} and voltage dependent collection, especially with increased S/(S+Se) front gradients. This suggests that the IEC baseline processes may not see a benefit from front S/(S+Se) gradients without increased minority carrier lifetimes.

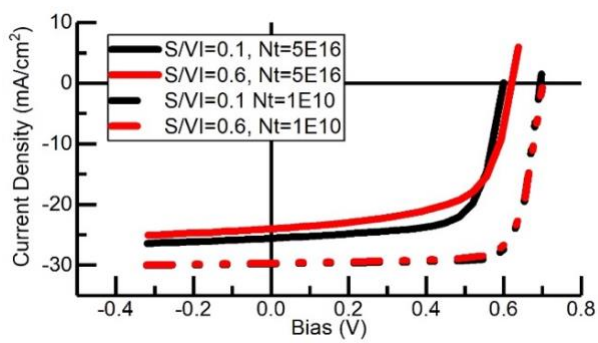

Figure 17. Simulated JV curves from SCAPS. Solid lines have deep trap concentrations of 5E16 cm^{-3}, and dashed lines have deep trap concentrations of 1E10 cm^{-3}.

To investigate the potential for increased V_{OC} attained by increased Ga content and E_g at the front of the absorber the reaction process was focused on high Ga precursors. Characterization of Cu-In-Ga precursors with Ga content increased to Ga/(In+Ga) = 0.5 showed that they exhibit the same phases as precursors with Ga/(In+Ga) = 0.25, but in varying quantity. In one experimental set to help understand composition control, precursors with Ga/(In+Ga) = 0.5 were selenized in a single reaction step for 90 minutes at temperatures from 425 to 500ºC. The resultant absorbers were characterized by EDS on the surface and at the back after delaminating from the Mo contact. All films showed Ga/(In+Ga) = 0.21 at the front and Ga/(In+Ga) ~ 0.7 at the back showing a pathway to control through-film bandgap gradients. In addition, these films had better adhesion that films with lower Ga reacted at the same temperatures.

To optimize the device behavior with respect to composition further efforts focused on optimization of the reaction of sputtered Cu-In-Ga precursors with Ga/(In+Ga) = 0.4 or 0.5 and Ag-Cu-Ga-In precursors with Ga/(In+Ga) = 0.4 and Ag/(Ag+Cu) = 0.05. Ga content was reduced from 0.5 to 0.4 to improve overall device performance, as higher Ga content has been consistently shown to increase voltage deficit and reduce collection. Ag was incorporated in small quantities to provide the benefits of accelerated reaction

kinetics and improved adhesion without higher Ag content than needed. The Ag-Cu-Ga-In precursors in a single-stage H_2Se reaction process at different selenization conditions to determine effect of the process on composition control. GI-XRD spectra at varying incident angles for three reaction conditions, 400°C-120min, 425C-90min, and 450°C-90min showed an increased peak shift from the lowest incident angle to the highest in GI-XRD indicitive of a increasing amount of Ga deeper into the film. Figure 18 shows symmetric (112) XRD spectra for single-stage H_2Se reaction conditions with increasing time and temperature from 400°C for 120min to 450°C for 90min. We observe increaseed peak broadening due to a stronger Ga gradient. Then after a certain reaction extent, in this case between 425C-90min and 425C-120min, two phases are formed and the composition no longer varies. SIMS composition profiles are shown in Figure 19 for the three of the reaction conditions and demonstrate the ability to tuen the compositon gradient. However, the Ga gradient for the 450°C sample, shows no evidence of a step that might be expected from the two-phase XRD resutls. This suggests that phase split is due to lateral phase differences between CIGS grains which may be harmful to device performance.

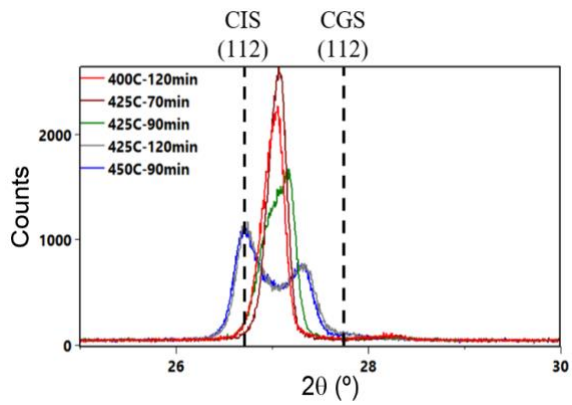

Figure 18. Comparison of symmetric XRD line profiles for various selenization conditions.

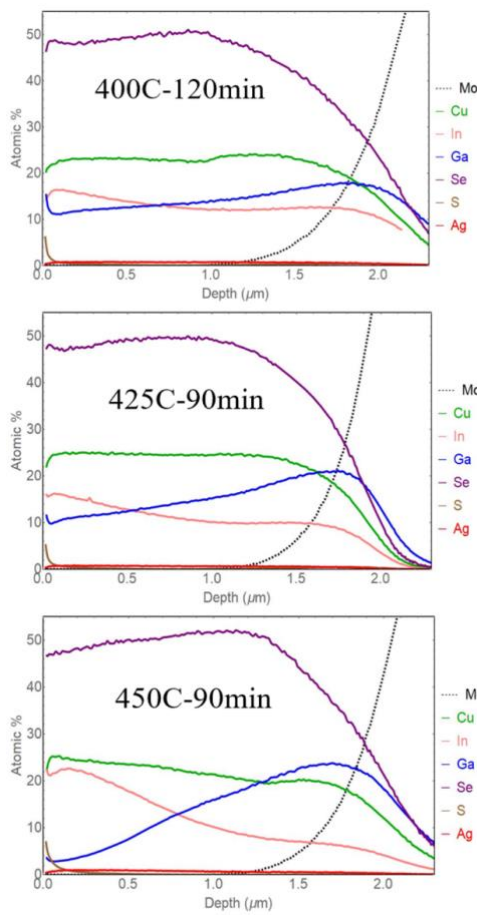

Figure 19. SIMS profiles of ACIGS films at varying selenization conditions.

A detailed study of reacted film morphology by scanning electron microscopy showed that the reaction conditions can be tuned to produce a large increase in grain size with different Ga contents. Furthermore, the sulfization stage was extended to longer times but with lower H_2S concentration to potentially reduce defects in the near-surface region of the reacted absorbers. This reduces the S gradient while extending it deeper into the film. Thus, we are able to control both the Ga and S profiles to observe the effect on device behavior and provide a wider range of composition profiles for the development of device models. Optimization of these processes led to the device results shown in Figure 20. The highest V_{OC} was achieved using a 50% Ga precursor, with device parameters V_{OC} = 707 mV, J_{SC} = 27.4 mA/cm^2, FF = 67.3, η = 13.1% (no AR-coating). High voltage and poor current

collection in this device led to the reduction of the Ga content to 40% and the addition of a small amount of Ag to improve adhesion. This led to a device with V_{OC} = 674 mV, J_{SC} = 33.1 mA/cm^2, FF = 71.4%, and η = 16.0% (with AR-coating). These are compared in Figure 20 to the highest efficiency baseline [Ga/(In+Ga) = 0.25] device from Budget Period 1 which had V_{OC} = 626 mV, J_{SC} = 34.2 mA/cm^2, FF = 74.5%, and η = 16.0%.

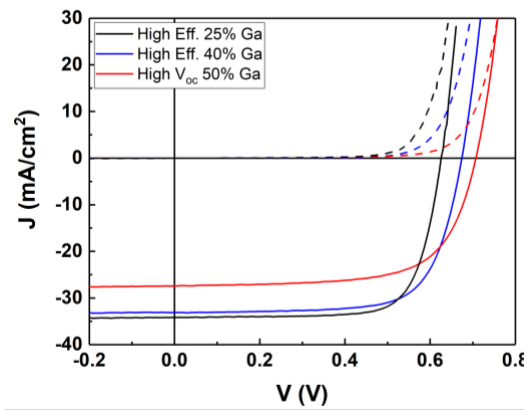

Figure 20. JV curves for devices with Ga/(In+Ga) = 0.25 (black), 0.4 (blue) and 0.5 (red).

One research sub-task that was not completed was an investigation of post reaction alkali treatments. Capability for controlled evaporation of KF and RbF were established to be utilized in a study of ex-situ treatments. These experiments were not completed because a reproducible set of films suitable for controlled experiments was not available in BP3 due to the project's refocus on RTP processing.

Rapid Thermal Processing

Due to relatively long reaction times on the order of hours using the standard selenization process, a rapid thermal process (RTP) was investigated. Using an RTP quartz lamp shown in Figure 21 heating and cooling times on the order of seconds can be achieved[22]. Additionally, total reaction time can be reduced to minutes.

The RTP reaction investigated for this project involved evaporating a layer of elemental Se on top of metallic precursors, then annealing them in Ar or H_2S ambient to form the reacted CIGS film. The standard reaction condition was a static reaction chamber charged with Ar to atmospheric pressure.

Figure 21. RTP lamp and reactor tube setup on the IEC H_2Se/H_2S reactor.

Initial RTP reactions involved 25% Ga/(In+Ga) precursors topped with an 8 µm thick capping layer of Se. These films were reacted for up to 20 min in Ar ambient at 600°C, and the film composition by EDS is shown in Table 4, along with the film morphology

shown in Figure 22. The surface of each film in this reaction set showed two distinct spots on the top and bottom of the film. By EDS, the Ga distribution in the middle of the films appears to be stronger than in the spots, which implies a difference in selenization reaction extent. This was believed to be caused by a difference in RTP lamp intensity in the different zones during the reaction.

Table 4. EDS composition for 25% Ga/(In+Ga) 8 µm films

EDS	L2047A-E11	L2047A-H11	L2047A-G11
Time	20min	10min	5min
		Middle	
Cu/(In+Ga)	0.91	0.93	0.92
Ga/(In+Ga)	0.05	0.05	0.05
Se/M	1.03	1.07	1.01
		Bottom Spot	
Cu/(In+Ga)	0.82	0.87	0.91
Ga/(In+Ga)	0.17	0.18	0.17
Se/M	1.10	1.10	1.03

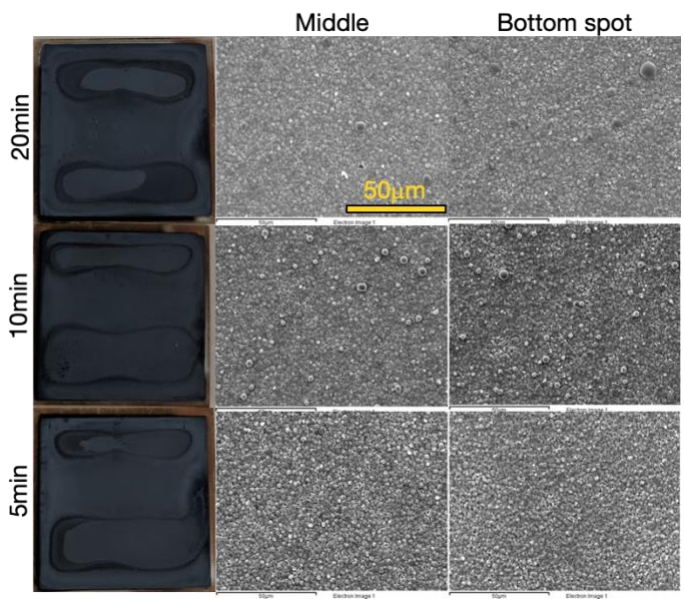

Figure 22. Film morphology for 5, 10, 20min reacted 25% Ga/(In+Ga) samples with 8 µm Se. Optical photographs of the entire 1”x1” sample in the left column show different spots and SEM images in the center and right columns show their morphologies.

Because of the relatively small heating area compared to the size of the samples, there is a significant temperature gradient from the center of the lamp to the sides of the reaction chamber just outside the heating zone. This temperature gradient causes eddy currents to remove hot gases from the reaction zone, meaning that any evaporated Se is immediately removed from the reaction zone. Because of this, the reaction only progresses with Se that remains deposited on the surface of the film, and once the Se cap layer has fully evaporated, the reaction stops. It was observed that due to the higher intensity heating on the top and bottom of the films, Se evaporated faster, resulting in a Se-deficient reaction condition and an underreacted film. Increased proportions of

precursor binary phases in the film promote additional recrystallization, which is consistent with the reduced Ga gradients observed in the higher intensity heating zones. By adjusting the lamp geometry, a more uniform (although still imperfect) heating distribution was achieved. Additionally, composition appears to be similar for all reaction times, confirming that no further reaction occurs after Se cap evaporation, which tends to occur around 1-2min of reaction time.

In an attempt to promote further recrystallization, 25% Ga precursors were deposited with 4 µm of Se and reacted in Ar. Based on the results of the previous section, reaction times of 5 min and 10 min were used, in addition to two additional ramp procedures, both with a total reaction time of 10 min. The 2-stage heating profile involves ramping to 300°C in ~1sec then holding for 5min, followed by an additional ramp to 600°C in ~1 sec which is held for an additional 5 min. The 5 min ramp procedure ramps to 600°C over 5 min, then holds at temperature for an additional 5 min. Front and backside EDS composition are provided in Table 5. For all reaction conditions, a near homogeneous Ga distribution is observed, implying high levels of film recrystallization. This is consistent with a reduced reaction extent caused by a reduction in Se availability, verifying that reaction extent can be controlled by the amount of Se provided.

Cross-sectional SEM images for 8 µm Se (middle spot) and 4 µm Se films are shown in Figure 23(a). In the 8 µm films, small grains are observed in all reaction conditions. Comparatively, the 4 µm films all have much larger grains, similar to that observed in high quality 3-stage selenized films. Of the 4 µm films the 5 min ramp condition appears to provide the largest grain size. In both the 8 µm and 4 µm samples, a low density of voids is observed near the back surface of the films, which is in contrast with the large void density commonly observed with the standard selenization process, showing that higher quality material may be achievable using the RTP process.

Table 5. Front and back EDS composition for 25% Ga/(In+Ga) with 4 µm Se-capping layers.

EDS	L2047A-A12	L2047A-B12	L2047A-C12	L2047A-D12
Time	10min	5min	2-stage	5min ramp
		Front		
Cu/(In+Ga)	0.94	0.91	0.93	0.93
Ga/(In+Ga)	0.22	0.21	0.21	0.21
Se/M	1.00	1.03	1.01	1.00
		Back		
Cu/(In+Ga)	0.85	0.77	0.68	0.80
Ga/(In+Ga)	0.25	0.24	0.21	0.24
Se/M	0.90	0.89	0.82	0.94

XRD profiles for the 4 µm samples are provided in Figure 24. A strong InSe peak (23°) is observed for all reaction conditions, which is incompatible with high quality devices[11]. The presence of InSe was not observed in the 8 µm Se samples. InSe remains in under reacted films, thus implying that the 4 µm Se condition, although yielding good film morphology, is insufficiently reacted for good device performance.

50% Ga/(In+Ga) films were also deposited with 4 µm and 8 µm of Se and reacted under the same conditions as 25% Ga/(In+Ga), EDS composition for 4 µm and 8 µm Se 50% Ga/(In+Ga) samples showed that for all 4 reaction conditions, the Ga/(In+Ga) measured by EDS is similar to the bulk value, implying a near homogeneous distribution resulting from strong film recrystallization. Comparing with the low Ga samples where the films appeared to be fully reacted with the 8 µm Se condition, recrystallization occurs at 8 µm in the high Ga films, implying that these samples react more slowly. Additionally, cross section SEM of the high Ga films in Figure 23(b) shows larger grains for both Se thicknesses compared to the 4 µm Se low Ga samples. Both of these results are consistent with the slower reaction and increased grain size observed with increased Ga in the standard selenization process.

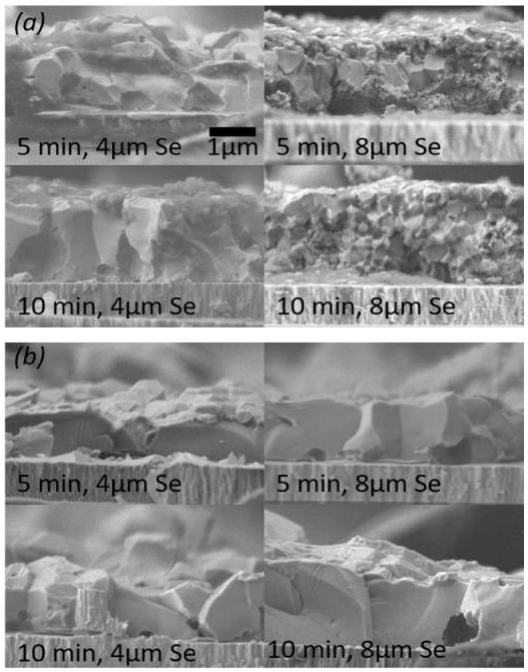

Figure 23. Cross section SEM images for (a) 25% Ga/(In+Ga) and (b) 50% Ga/(In+Ga) samples with 6 µm Se.

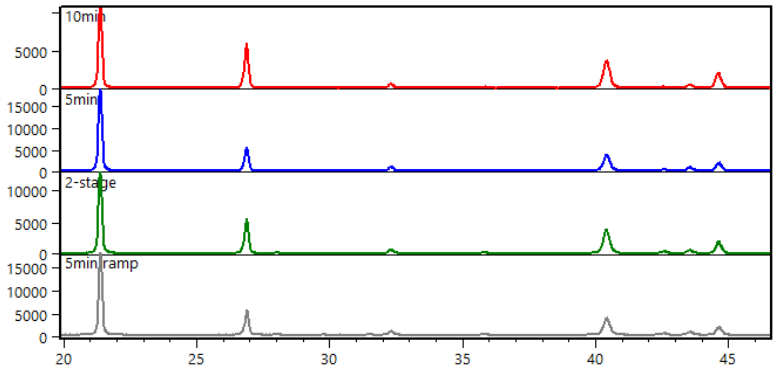

Figure 24. XRD profiles for various 4 µm Se 25% Ga/(In+Ga) reacted samples.

To verify that the high Ga films were undergoing slower reaction kinetics, and that a further reaction extent could be achieved through a thicker Se layer, 50% Ga/(In+Ga) precursors were deposited with a 16 µm Se capping layerand reacted. EDS composition provided in Table 6 show a reduction in Ga/(In+Ga) at the surface due to the formation of a Ga gradient. This result is consistent with the Ga gradients observed in the 25% Ga/(In+Ga) samples at high Se thickness, however, for the 50% Ga/(In+Ga) samples a higher Se thickness must be used to achieve the same reaction extent due to reduced reaction speed.

Table 6: EDS composition for 16 µm Se, 50% Ga/(In+Ga) films

EDS	16 µm Se	
Time	5min	10min
Cu/(In+Ga)	0.91	0.22
Ga/(In+Ga)	0.87	0.21

RTP Sulfur Reactions

Besides increasing the Se thickness, it is possible to increase reaction extent through the addition of S to the film. In this work two different S-incorporating processes (shown schematically in Figure 25) were investigated. The “static” process involves charging the reaction chamber with H_2S in Ar before the temperature ramp, thus exposing the film to H_2S ambient for the duration of the reaction. The “flowing” process utilizes an additional 5 min stage at the end of the standard static reaction in Ar, in which H_2S is flowed with Ar over the sample. Initial S reactions were carried out with a concentration of 0.35% H_2S for a nominal 10 min reaction in Ar for both Ga concentration films with a 4 µm Se capping layer and the compositions are shown in Table 7. Comparing the Ga/(In+Ga) compositions at the front and back of the film shows near homogeneous distributions for all samples , which is consistent with the films being underreacted due to low Se availability. Additionally, both the low and high Ga samples show large amounts of S, and in the case of the high Ga films, an apparent homogeneous through film S distribution.

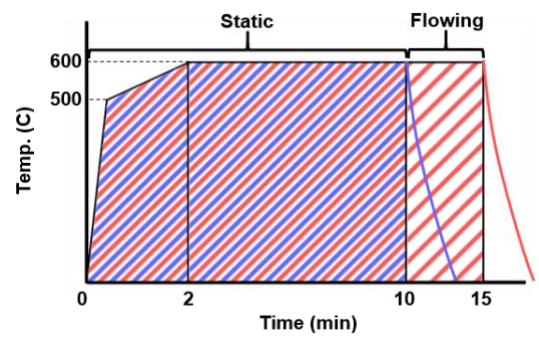

Figure 25. S reaction profile for (blue) static, and (red) flowing conditions

Based on the previous results, precursors with 6 µm Se were prepared for both Ga compositions and reacted with various S conditions. Compositosn for the 25% and 50% Ga/(In+Ga) reacted samples are shown in Table 8 and Table 9 respectively. In addition to the standard 10min static and flowing S reactions, these films were also reacted for 5 min and 20 min, and for 10 min in reduced H_2S concentration (0.035%). Looking at the 25% Ga/(In+Ga) results, similar Ga distributions were observed for all reaction conditions, which yielded a relatively flat Ga profile. The primary difference between the various conditions is the S uptake. For the 10 min standard reaction, the S uptake for the static condition was nearly double that of the flowing condition. This is likely due to the availability of the S during the reaction process in the static condition, causing more S to be incorporated as a reactant, whereas the primary S incorporation mechanism in the

flowing condition is substitution of S for Se in the already reacted film. Comparing to the 10 min reaction with low H_2S concentration, the S uptake did not change for the flowing condition but was reduced in the static condition. This result further verifies the hypothesis that S uptake in the flowing reaction is controlled by the reaction extent of the film, whereas S uptake in the static condition is controlled by S availability.

Table 7. Front and back EDS composition for 25% and 50% Ga/(In+Ga) films with 4 µm Se, reacted with H_2S.

EDS	Low Ga		High Ga	
Condition	10min Static	10min Flowing	10min Static	10min Flowing
		Front		
Cu/(In+Ga)	0.94	0.91	0.62	0.61
Ga/(In+Ga)	0.21	0.20	0.56	0.58
Se/M	0.99	1.00	1.13	1.21
S/(S+Se)	0.31	0.29	0.39	0.29
		Back		
Cu/(In+Ga)	0.91	0.83	0.58	0.69
Ga/(In+Ga)	0.27	0.26	0.53	0.54
Se/M	0.97	0.97	1.25	1.16
S/(S+Se)	0.15	0.05	0.40	0.32

Table 8. EDS composition for various 25% Ga/(In+Ga) 6 µm Se, S conditions.

Condition	10min, static	10min, flowing	10min, 0.035% static	10min, 0.035% flowing	20min static	20min flowing	5min static	5min flowing
Cu/(In+Ga)	0.83	0.83	0.90	0.90	0.82	0.87	0.87	0.88
Ga/(In+Ga)	0.19	0.18	0.21	0.20	0.20	0.18	0.20	0.20
Se/M	1.02	1.07	0.99	1.16	1.01	1.10	0.98	1.03
S/(S+Se)	0.15	0.07	0.08	0.07	0.26	0.13	0.15	0.17

Table 9. EDS composition for various 50% Ga/(In+Ga) 6 µm Se, S conditions.

Condition	10min, static	10min, flowing	10min, 0.035% static	10min, 0.035% flowing	20min static	20min flowing	5min static	5min flowing
Cu/(In+Ga)	0.83	0.85	0.90	0.84	0.82	0.83	0.85	0.85
Ga/(In+Ga)	0.49	0.50	0.51	0.48	0.50	0.47	0.52	0.51
Se/M	1.00	1.09	1.03	1.10	1.07	1.09	1.06	1.09
S/(S+Se)	0.25	0.12	0.03	0.08	0.28	0.03	0.24	0.20

S uptake is also increased for the 20 min static reaction time, which is consistent with a longer reaction time in the presence of S. Comparing the flowing reaction conditions at various times shows that the S uptake tends to vary depending on the total reaction time before S is introduced. Previous results without S showed that the CIGS reaction stops progressing after the first 1-2min of the anneal, thus significant changes in phase composition would not be expected at longer reaction times. However, based on the flowing S results, there appears to be changes in phase or composition that occur with increasing reaction time that effect the degree of S uptake after the reaction.

The primary trends observed for 25% Ga/(In+Ga) samples are also observed with 50% Ga/(In+Ga). All of the high Ga reaction conditions show near homogenous Ga distributions, and a wide range of S uptakes were observed. The 10 min static and flowing reactions for high Ga resulted in higher S uptake compared to low Ga, which is consistent with a lower reaction extent due to Se from the slower reaction speed. Comparing the static reactions, there is little change in S uptake between reaction times. Because these 50% Ga/(In+Ga) precursors with 6 µm Se are reacting in a Se-deficient condition, it is likely that the films remain partially unreacted still after reaction with the charged H_2S is completed. It is expected that if a higher concentration of H_2S was used, the higher reaction time films would have resulted in increased S uptake, as there would still be H_2S present after the films are fully reacted to participate in substitution of Se. Additionally, there is a wide range of S uptake values for the flowing reactions, with the lowest uptake for 20min and the highest for 5min. The reason for this difference is likely some kind of phase adjustment or evolution in longer total reaction times similar to what was observed with low Ga, but the specific changes that occur remain unclear.

RTP Device Results

Initial devices were made for 4 µm Se 25% Ga/(In+Ga) samples, which resulted in generally poor performing devices, with the best cell JV curve shown in Figure 26(a) (V_{oc} = 488 mV, J_{sc} = 19.1 mA/cm^2, FF = 41.6%, Eff. = 3.9%). The best performing sample was a 10 min reaction that used the flowing S process. By incorporation of S, the InSe that would normally be present for this reaction condition was eliminated, enabling the production of a functioning device. However, due to the high amount of S uptake in this film, the current blocking effect was observed. Additionally, due to remaining non-uniformity in the RTP lamp system, there is lateral variation in composition and reaction progression throughout the film, which results in poor overall device performance for cells with large area relative to the total sample area.

Devices were also produced for 25% Ga/(In+Ga) precursors with 6 µm Se, and the best cell JV curve is shown in Figure 26(b) (V_{oc} = 463 mV, J_{sc} = 27.4 mA/cm^2, FF = 45.5%, Eff. = 5.8%). The best device from the 6 µm set came from a 10 min reaction with the static S condition. This sample had reduced S uptake when compared to the 4 µm Se device, however the S composition was still relatively high when compared to well behaved standard selenization devices. Although device performance was improved, this sample still heavily underperforms what is expected of a film with this composition.

Based on previous results and issues with heating uniformity, it was hypothesized that a primary source of device performance loss was non-uniformity over the cell area. To test this, the 6 µm Se best cell was divided into many small area devices (A ≅ 1mm^2). Due to the nature of the dividing process and the resulting small size of the new devices, it is difficult to measure an accurate cell area and thus difficult to get accurate measurements of J_{sc}. However, V_{oc} and FF both remain accurate for the small devices and Figure 27 shows heat maps for FF and V_{oc}. These results show non-uniformity in device performance across the larger cell area, and that the majority of the small area cells exceed 500 mV V_{oc} and 60% FF. The best small area cell resulted in V_{oc} = 591 mV, and FF = 65.7%, surpassing the overall cell performance by over 100 mV and 20% FF. This test verifies that high quality material is produced through the RTP process, however, heating non-uniformity decreases device performance.

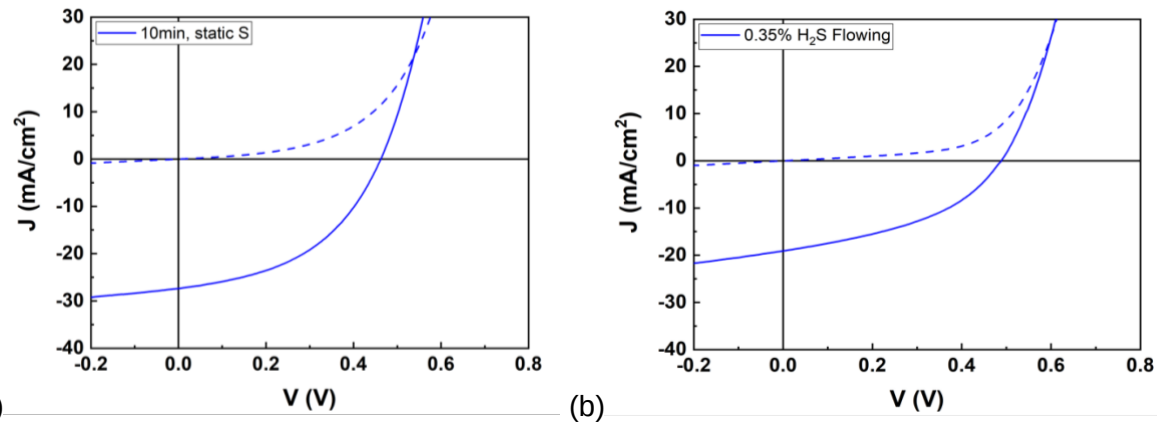

Figure 26. JV curves for (a) best performing 25% Ga/(In+Ga) 4 µm Se cell and (b) best performing 25% Ga/(In+Ga) 6 µm Se cell.

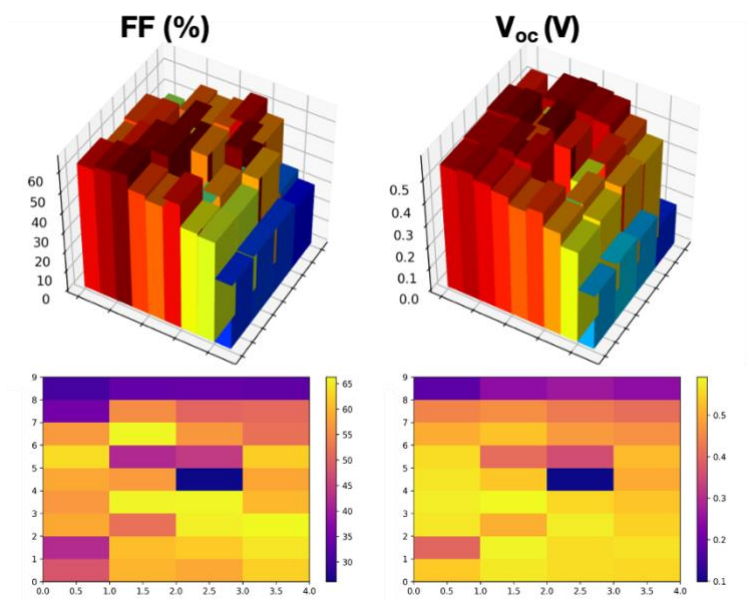

Figure 27. Topographical and top-down view heat maps for FF and V_{oc} of small area cells

50% Ga/(In+Ga) devices for the 4 µm and 6 µm Se conditions resulted in generally poor performance, due to under reaction of films and large amounts of S uptake. Based on the 50% Ga/(In+Ga) RTP results, increased Se thickness must be used to accommodate the decreased reaction speed at high Ga compositions, thus 50% Ga/(In+Ga) precursors were deposited with 12 µm of Se and reacted. The best performing cell for this condition set had V_{oc} = 474 mV, J_{sc} = 31.7 mA/cm^2, FF = 52.8%, and Eff. = 7.9%. This device was reacted using the flowing S condition, although a similar Eff. = 7.8% cell was produced using the static S process. Current blocking effects are reduced in this device compared to the previous 25% Ga/(In+Ga) ones, likely due to a more modest S uptake, pointing out further room for Se thickness and S process optimization.

In a further attempt to improve film uniformity and to verify that the issue had to do with the RTP lamp setup, a new RTP approach was developed using the standard selenization heating jacket. In the standard process, samples are ramped within the hot zone of the

jacket, however ramping to 600°C with this process takes ~45 min. To approximate the RTP heating system, the jacket was left to ramp with no samples inside until the temperature stabilized at 600°C. The samples were then quickly pushed into the hot zone, allowed to react for 10 min, then removed, allowing for heating and cooling on similar time scales to the RTP lamp. The benefit of this process is that the heating jacket provides a more uniform hot zone, and thus should eliminate the uniformity variable from device performance. This test was performed on a 6 µm Se 25% Ga/(In+Ga) sample and used a static H_2S condition. The resulting best performing cell JV curve yielded V_{oc} = 447 mV, J_{sc} = 33.8 mA/cm^2, FF = 60.3%, Eff. = 9.1%. Compared to the RTP lamp devices, performance was improved, especially in current collection. Based on previous results from this project, samples with a Ga gradient that is too strong tend to have reduced device performance, and specifically a drop in V_{oc} (which may be correlated to effects from over-selenization), and it appears that the Ga gradient observed by EDS in this film may have contributed to the low V_{oc} in this sample. Due to the larger and much more uniform hot zone inside the heating jacket, Se vapor is not removed from the film reaction area at the same rate that it is in the RTP lamp system. Because of this, the effective Se availability is increased, resulting in a further reacted film. However, the improved performance still helps to verify that improving heating uniformity would resolve device performance issues, and with further Se thickness optimization in this heating system even better devices could be made.

In summary of the RTP work, 25% and 50% Ga/(In+Ga) precursors were topped with various thickness of elemental Se and reacted using RTP to form CIGS absorbers. It was observed that due to rapid removal of Se vapor from the reaction zone, reaction extent is controlled by the amount of Se that is evaporated onto the precursor. 50% Ga/(In+Ga) films appear to react slower yet produce larger grain films, which is consistent with previous work using standard selenization. Due to this high Ga films require additional Se thickness to reach desired reaction extents when compared to low Ga. It was also shown that the void density at the back of the film could be significantly reduced with the RTP process compared to standard, slow reaction processes. S was incorporated into films using two primary methods, and it was observed that a wide range of S uptake can be achieved by adjusting the S condition and total reaction time. Devices produced with RTP samples are still under performing, but it appears that the primary reason is due to film non-uniformity. Additionally, based on initial results with different Se thickness on both 50% and 25% Ga/(In+Ga) precursors, it appears that with further optimization and improved heating uniformity, high quality devices are achievable using this process.

III. Materials characterization

Time resolved photoluminescence is a non-destructive method to measure the decay dynamics of photoexcited electrons in semiconductors. It is known that the increased lifetime is correlated with open-circuit voltages of solar cells and hence is an indicator of the quality of solar cell material. Using our previous expertise on building custom microscopes to map carrier lifetimes using two-photon time-resolved photoluminescence (2P-TRPL), in this project we have developed and demonstrated the capability to map carrier lifetime in CIGS PV films.

Due to the small bandgap of CIGS materials, we are not able to use traditional optics and detectors to measure the photoluminescence of these samples. Thus, we have developed a custom microscope designed to map spectra and lifetime on CIGS samples that emit light in the near infra-red (NIR). Unlike the previous two-photon microscope which was based on a commercial optical microscope, this microscope has been designed from individual components that give the flexibility to use optical elements designed for NIR operation. We have also incorporated dual excitation paths, one for 1P- and another for 2P- laser excitation.

Signal to background ratio is significantly worse for IR detectors compared with visible light detectors. This means that large 3D scans may be impractical and will limit the volume of data we can acquire, especially for samples with poor luminescence performance. Mapping of carrier lifetime in CIGS involves the following challenges. The ability to detect low signal is critical to measure the optoelectronics properties at low laser power, which is worth striving for at least three reasons: (1) The interpretation of data acquired in the low injection regime, where the PL intensity is linear to the excess carrier concentration, is more feasible than in other regimes, (2) low laser power generally are closer to working conditions of solar cell and (3) high laser power may alter or damage the sample through ablation.

We have hired Benedikt Ursprung as a graduate student in the Mechanical Engineering department at Columbia University. Benedikt has had extensive experience in two-photon microscopy applied to photovoltaics. His master's thesis focused on the development of 2P-TRPL for CdTe 3D lifetime tomography and was a co-author of our previous publication in Advanced Materials[23].

During this project, we have measured samples from different collaborations including samples from the IEC, Stion Inc, and ZSW (Zentrum für Sonnenenergie- und Wasserstoff-Forschung, Germany) through a collaboration with Prof. Shubhra Bansal at the University of Las Vegas.

Microscope Development and capabilities

We have built a custom microscope that measures NIR photoluminescence and lifetime of PV samples. It allows for 2D and 3D mapping of these optical properties. This microscope measures photoluminescence in epifluorescence (reflection) mode and can measure either the time dynamics (lifetime) or spectrum of the light emitted from the sample. During this project, the microscope had been improved a number of times based on our experience measuring CIGS samples. The final schematic of the microscope is provided in Figure 28. The main improvements from the original design include:

1. the collection and excitation path are the same for 1P and 2P excitation such that the collection path transmits the beam splitter/dichroic unit. This omits the realignment of the detectors when a beam splitter or dichroic is replaced.
2. the number of optics in the collection path was reduced to increase collection efficiency.
3. Shielding to reduce ambient light noise.

We have incorporated two detectors into the system to measure spectra and lifetime for IR emitting materials. For spectral measurements, we have attached a Princeton Instruments OMA:V InGaAs spectral camera that can measure light with wavelengths out

to 1.7µm to our monochromator. However, due to malfunction, the OMA:V was later replaced with an Andor iDus InGaAs detector. For lifetime measurements, we use an MPD InGaAs Avalanche Photodiode with sensitivity out to 1.7µm and a timing resolution of <100ps.

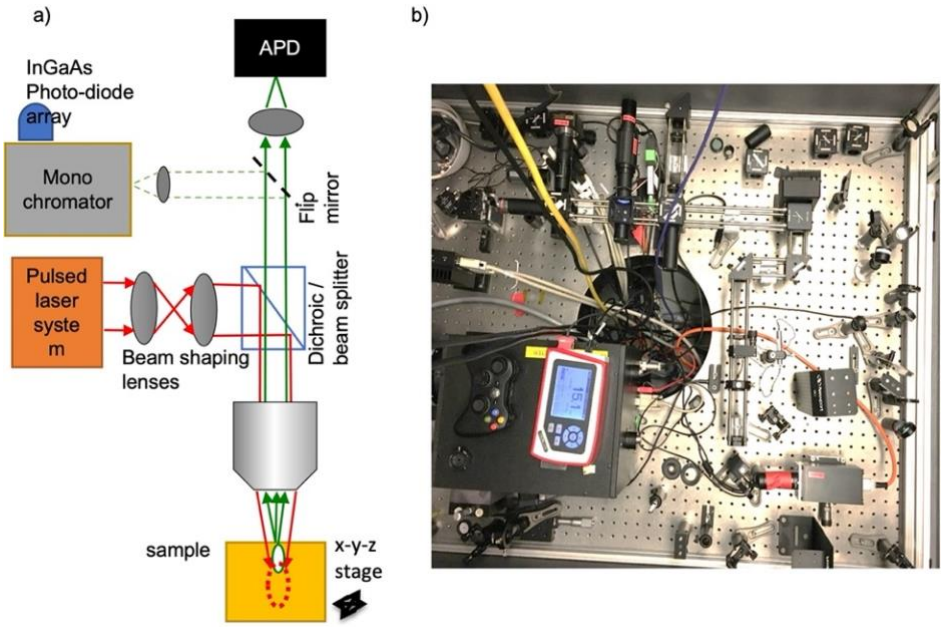

Figure 28**.** a) Schematic of the NIR 2P TRPL microscope built for this project. B) Photograph of microscope.

Long lifetime tail reveal mechanism at different times scales

The repetition rate of the laser limits the maximal measurable lifetime of the system (see Figure 29). An example of a decay that is not fully recorded is shown in Figure 30 a which was acquired with a Ti:Sapphire femtosecond pulsed laser with a repetition rate of 80MHz. This high repetition-rate limits us to measuring PL decays that are shorter than 12.5ns. Therefore, we have added two laser systems to the setup which allow us to measure PL decays. First, we acquired a 640nm pulsed laser with nanosecond pulse widths that allow one-photon excitation measurements, and which can map the whole PL decay (see Figure 30 b). However, the pulse width of the 640 nm laser is around 4 ns, which limits time resolution and hides the fast, sub-ns, components of the decay dynamics.

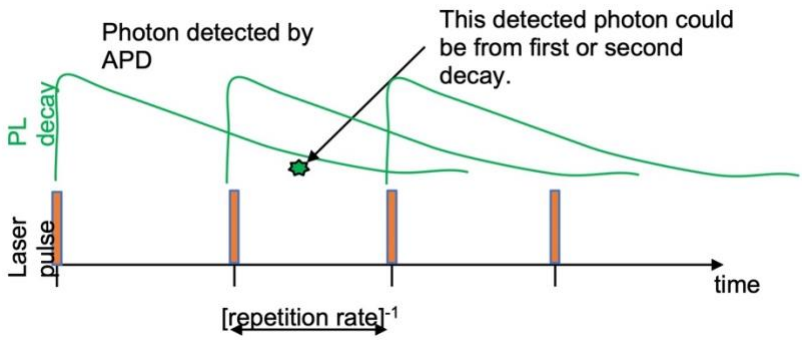

Figure 29. Illustration of how repetition rate limits the maximal measurable lifetime. After a laser pulse (indicated by bottom time series) excites electrons in the sample, the electrons decay by emission of photon according to a PL decays as indicated by the top lines. If these decays are longer than the repetition period, then it is impossible to attribute a detected photon to an excitation pulse.

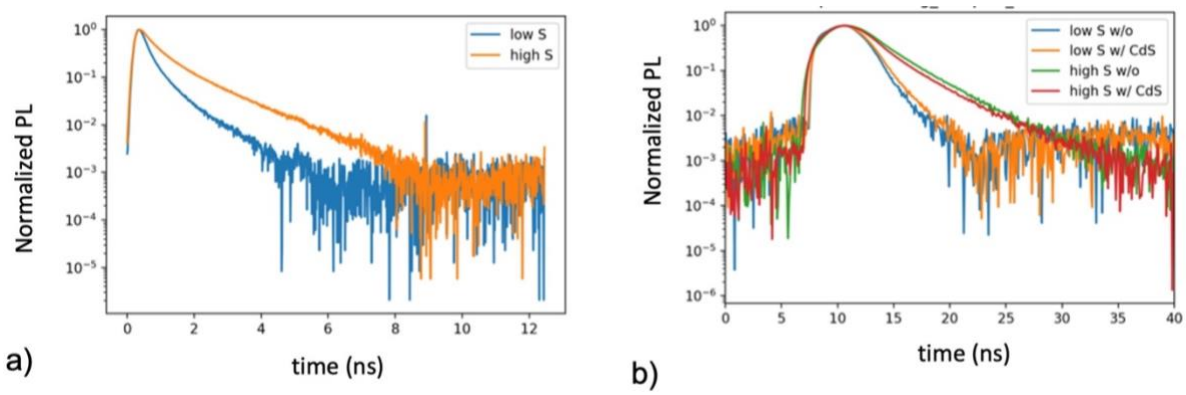

Figure 30. High vs low Sulfur (S) content in CIGSS. a) was acquired with 80Mhz Titanium-Sapphire laser. 100 ps decay dynamics can be resolved as the pulse width is on the order of femtoseconds. Note, that the decay of the low S sample is not completed. b) acquired with 640 pulsed laser diode revealing the long tale of the high S sample. The ns second pulse width hides the fast decay dynamics.

TRPL and Hyperspectral maps reveal inhomogeneity

To map carrier lifetime throughout the sample we have added an Attocube 3-axis translation system that provides 50 nm repeatability over a 25 x 25 x 25 mm^3 volume. This will allow us to repeatably measure many disparate locations on a large PV sample. Figure 31 a) shows a typical lateral scan on an IEC CIGS absorber sample. Dark and bright regions correspond to low and high lifetime regions, respectively. The length scale of these heterogeneous regions is ~2-7 µm which is much larger than the grain size (<1.2 µm, cf. topographical AFM in Figure 31 c) for these samples. We observe such inhomogeneities in a lifetime in all samples from all collaborators that we have measured to date. The origin of these dark regions was not understood and was further investigated with KPFM measurements (see below).

Depth profiling for lifetime

To explore the lifetime trends throughout a graded CIGSS film we have implemented several approaches:

1. Measuring cross-section samples
2. Use 2P lifetime measurements with wavelength filtered collection to collect from bandgap graded samples
3. Use excitation wavelength-dependent 1P lifetime measurements that probe deeper into the film with longer excitation wavelengths

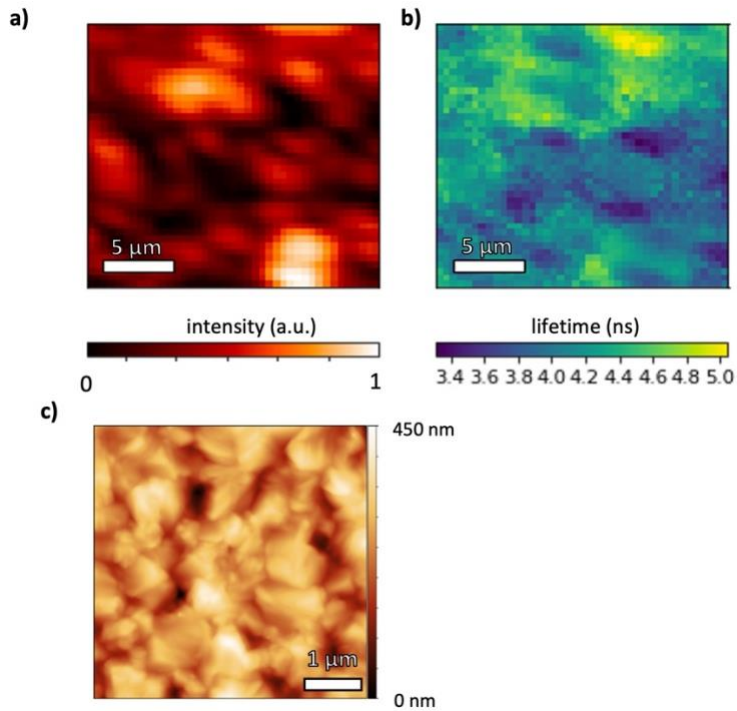

4.

5. Figure 31. Scan on Cu(InGa)SeS$_2$ sample from IEC. (a+b) the lateral intensity and lifetime map using an 1100-10 nm bandpass filter. c) topographical AFM image indicating the size of the grains to be smaller than the inhomogeneities seen in a and b.

Unlike our success with thicker CdTe films were we able to use two-photon excitation - TRPL, CIGSS films are difficult to directly image in depth. With 2P-TRPL, using sub-bandgap photons, excitation in confined volume subsurface. However, for these thin CIGSS (~1.8 µm) samples, the depth resolution for confocal microscope given by

$$r_{axial} = 0.89\,\frac{n\lambda}{NA^2} = 2.1\,\mu m$$

(assuming highest numerical aperture $NA = 0.95$ available, emission wavelength $\lambda = 1300\,nm$ and index of refraction $n = 1.7$ for CIGS) is too low to resolve gradients in the film. Therefore, we are following three different approaches.

First, to address lifetime at a different depth, we excite throughout the film and use bandpass filters to discriminate emission from different depths (Figure 32 a) as deeper into the film the bandgap increases and therefore emission wavelength. A second approach, the sample is cleaved and broken und subsequently we measure the cross-section directly as sketched in Figure 32 b). Note that depth direction now maps to a lateral dimension. This is advantageous as the theoretical lateral resolution given by

$$r_{lateral} = 0.4\,\frac{\lambda}{NA} = 0.55\ \mu m$$

is improved significantly using the same parameters. This should allow distinguishing between features in the film.

Third, the penetration depth of a laser beam increases for higher energy photons. By changing the excitation wavelength, we can steadily probe deeper into the sample as illustrated in Figure 32 c).

We have performed measurements using these approaches. Figure 33 a) shows time traces measured with different filters. We find that lifetime decreases for bluer photons, which is unexpected as lifetime usually increases away from the surface and the bandgap increases along with depth. Second, we have fabricated a new sample holder which allows exposing cross-sections to excitation and emission beams. Figure 33 b) and c) show the intensity and lifetime maps from scans on a CIGS cross-section measured after cleaving and breaking the sample. Thus far, we are not able to resolve bandgap differences along with film thickness.

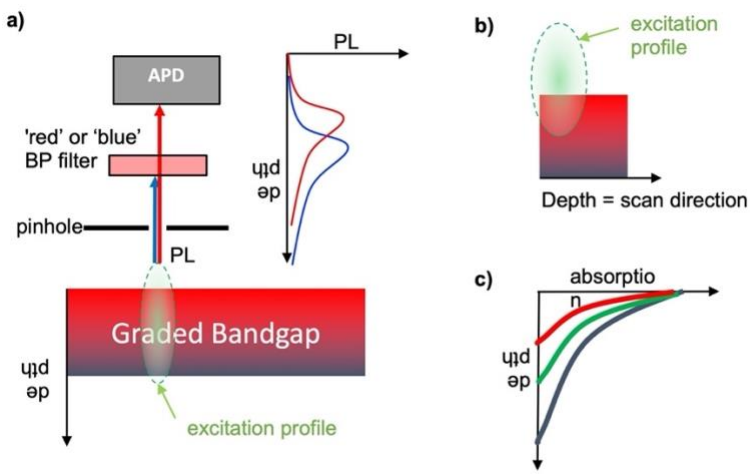

Figure 32**.** Approaches to extract depth information. a) channeling the PL emission. b) cross-sectional scans. c) tuning excitation wavelength.

1 photon vs 2 photon absorption reveal higher lifetime in bulk

A fourth approach of “depth profiling” is comparing 1P vs 2P excitation PL lifetime. We expect the surface-sensitive 1P excitation to yield faster initial decay as the surface generally contains more defects levels than the bulk. Indeed, we find the initial decay for 1P to be faster than for 2P (FFigure 34 a). Furthermore, within this short time window of the measurement, the slower component of the decay is measurable indicating PL from further away from the surface. On the other hand, we find that the 2P reveals decay with a rather mono-exponential behavior within this probe time, which indicates that the influence of the defect-rich surface is not as prominent as for the 2P measurement.

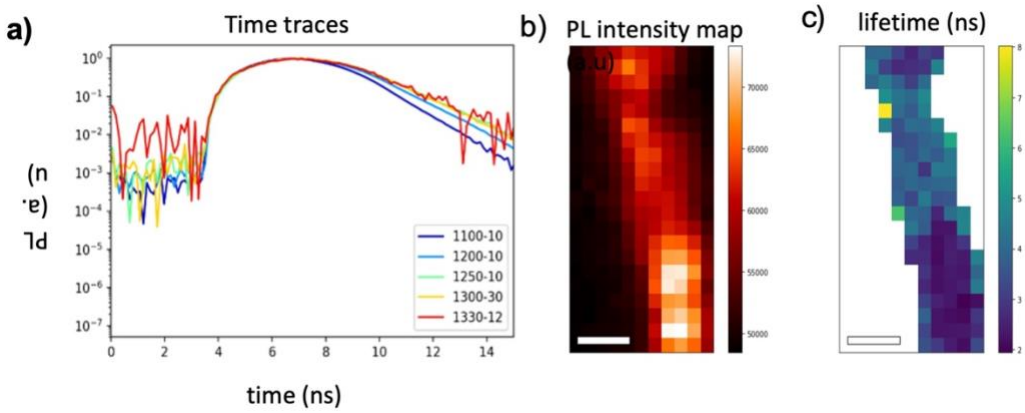

Figure 33. Initial results for acquiring depth information. a) channeling PL with different excitation wavelengths. b) and c) are intensity and lifetime maps from scans on a CIGS cross-section. Scale bar is 2 µm.

Note, that the averaged lifetime

$$\tau_m = \frac{A_0\tau_0 + A_1\tau_1}{A_1 + A_2}$$

and the slow component τ_1 are somewhat more similar for both measurements which indicates that the 1P measurements probe a substantial part of these thin films.

Finally, we have confirmed that we observe two-photon PL emission from our CIS test samples. Shown in Figure 34 b), we have measured the intensity of PL emission vs laser IR input power (1600nm) (*I*) and observe a super-linear dependence close to I^2, indicating a non-linear optical effect, i.e. two-photon absorption, and PL.

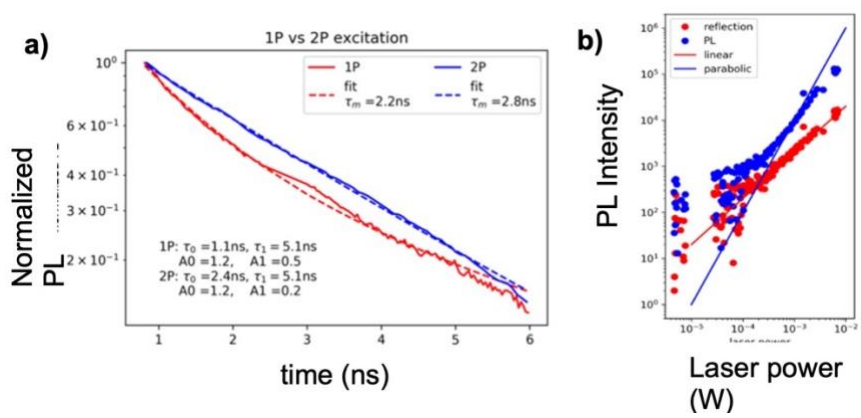

Figure 34. 1P vs 2P excitation TRPL on ACIGS film with biexponential fit b) Two-photon PL power dependence with 1600nm pulsed laser excitation. Blue data is from PL ~1200nm and red data is laser reflection.

Effect of light Na concentration on Heat and Light Soaking

In collaboration with Shubhra Bansal at UNLV, we have worked to measure time-resolved photoluminescence changes as a function of stress testing including heat and light soaking. This work is currently submitted and under review for publication[24].

In this work, we investigated the effect of heat, light, and voltage bias on metastable behavior of CIGS solar cells through an accelerated stress test in accordance with the thin-film PV stabilization tests in IEC 62215-2 standards. These stress tests included light soaking, that is, exposure to solar simulator light (AM1.5 G spectrum, 1000 W/m^2 radiation), at 85° C for 50-100 hours. The effect is investigated for CIGS with different Na concentration levels.

Several groups have reported an increase of open-circuit voltage under light soaking and an increase of carrier density. Erslev. et al[25] observed an increase in carrier density in Na containing devices after light exposure, but no increase in carrier density in Na-free CIGS devices. Na treatments in CIGS are known to increase the CIGS-efficiency due to an increase in p-type conductivity. It is hypothesized that doping in Na treated samples are due to the introduction of shallow acceptor defects, elimination of In_{Cu} compensating donors, or elimination of defects at grain boundaries and surface passivation. Theoretically, the amphoteric V_{Se}-V_{cu} divacancy model predicts that the incorporation of Na leads to an increase of carrier density as well as defect states. However, the introduction of these defects generally shortens its carrier lifetime.

To study the effect of Na levels and accelerated stress test (AST), two types of devices were fabricated at ZSW, Germany, and analyzed with lifetime measurements and time-of-flight Secondary Ion Mass Spectroscopy (ToFSIMS). Type 1 has a baseline Na concentration and for Type 2 the Na concentration was reduced during growth and has an additional Na diffusion barrier layer bellow the Molybdenum back contact to reduce the Na diffusion from the glass substrate (Figure 35 a). We took reference TRPL and ToFSIMS measurements without AST, performed AST on sister devices under two different voltage bias conditions: under open (OC) and closed circuit (V=0), and finally compared to equivalent data acquired on post-AST devices.

ToFSIMS data,shown in Figure 35 c) confirms the reduced Na concentration for Type 2 throughout the device. Initially, particularly for Type 1, the Na concentration is significantly higher towards the back contact and somewhat reduced toward the front contact. AST pushes Na toward the front contact leaving the Na profile somewhat more homogeneous. This Na accumulation was found to happen primarily at grain boundaries.

TRPL measurements at the Molecular Foundry reveal a decrease in minority carrier lifetime for Type 1 devices after AST under both conditions. This is consistent with previous reports indicating lower lifetimes with increased Na concentration. Conversely, we find that for the Type 2, lifetime slightly increased under short circuit condition, where the Na level slightly increased compared to the non-AST device. Under open-circuit conditions, however, the lifetime decreased almost to levels of high Na devices, although the Na level is 2-3x lower than in Type 1 devices. We also note the highest Oxygen levels (Figure 35 d) in this device. Perhaps, the low carrier lifetime in this device can be attributed to the high O level, as O is known to form shallow O_{Se} acceptor defects in CIGS. We also note that the Zn levels for OC Type 2 device were also reduced (data not shown).

Finally, consistent with previous reports, the Na richer Type 1 devices perform better than the Na poor Type 2 devices which indicate that the increased conductivity due to p-type doping of Na outcompetes the detrimental reduced lifetime. This data set indicates that

Na impacts lifetime for CIGS considerably and those other elements like Oxygen also play important roles.

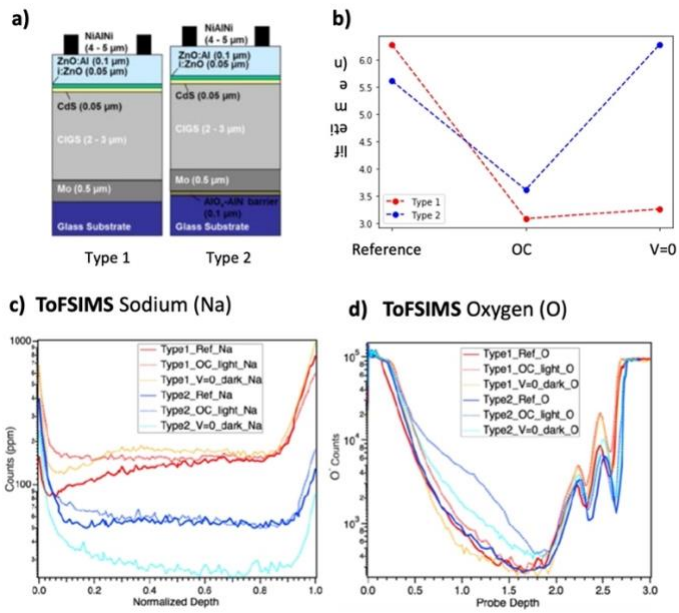

Figure 35. a) Schematic of Type 1 and Type 2 devices. Type 2 has an additional alkali diffusion barrier layer. b) lifetime fit for both samples under before (Ref) and after open circuit (OC) and short circuit (V=0) conditions, c) Na vs and d) O levels vs depth acquired with ToFSIMS. ToFSIMS were acquired in ZSW and TRPL measurements at the Molecular Foundry.

Effect on sulfur content on samples

As noted earlier in Figure 30, a CIGSS sample with high S content had a longer lifetime than a sample with Low S. We investigated lifetime on a sample set from IEC with various Sulfur content (0%, 2%, 12% [S]/[Se+S]), see Figure 36. This measurement confirmed that lifetime is increased if Sulfur is incorporated, however, the 2% have shown slightly higher lifetime compared to 12%. Also, we find that sulfur decreases surface roughness.

Correlation with KPFM

To understand the origin of the 2-7 µm inhomogeneity we were also looking at combining lifetime measurements with other complementary techniques. For example, we worked Ravi Chintala, a post-doctoral fellow in Paul Ashby's group at the Molecular Foundry, who focuses on mapping work functions in CIGS materials using illuminated Kelvin Probe Force Microscopy (KPFM). Illuminated KPFM is an AFM based technic that measures charge accumulations on illuminated surfaces. Charge trapping and entrapping is believed to affect the long tail of the lifetime traces and leaves a signature in illuminated vs dark KPFM scans. Using KPFM we also found inhomogeneity on the order of 2-7 µm. To correlate the two characterization methods we used fiducial markers, see Figure 37. However, we were not able to directly correlate lifetime with the signal from illuminated KPFM Figure 37 d).

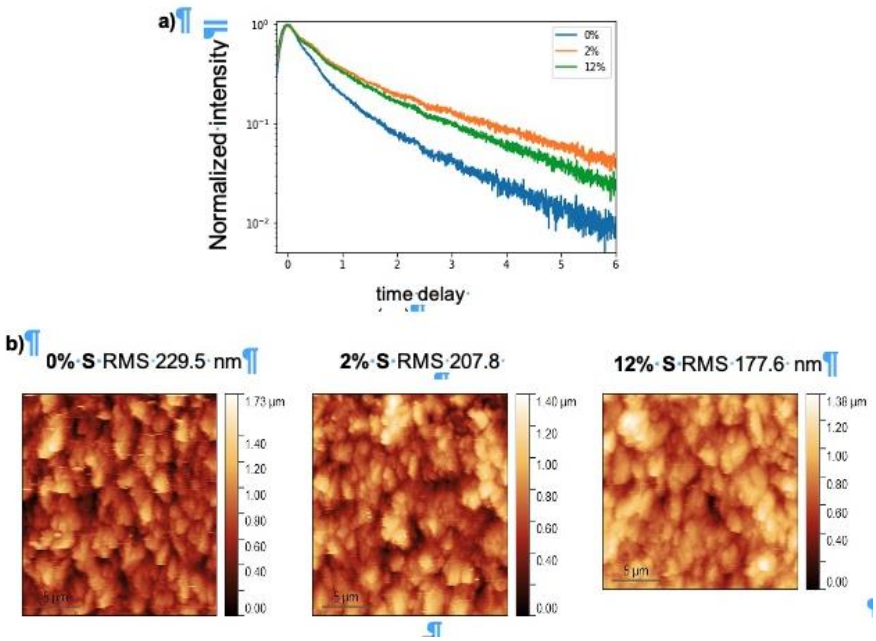

Figure 36. a) Effect of sulfur content on lifetime indicating that highest lifetime is achieved on a 2% cell. b) AFM morphology of the three samples.

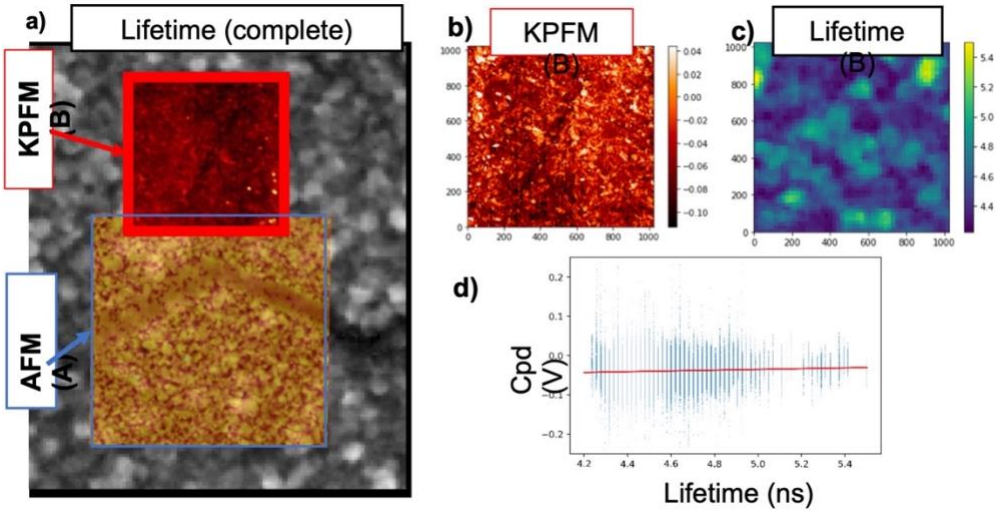

Figure 37. a) Overlay of two KPFM maps on a larger PL map. Note the fiducial marker used to align an AFM height map (A) with the PL map. The KPFM map (B) was acquired with the same AFM, which allowed accurate alignment to the AFM map (A). b) and c) are the overlaid maps to generate the correlation in d) lifetime and KPFM contact potential difference (Cpd) signal.

In summary of this task, we successfully built a custom IR microscope capable of measuring and mapping photoluminescence and carrier lifetime of CIGS materials and variants. By collaborating with several CIGS PV research and development groups we have demonstrated that lifetime strongly depends on the chemical composition and general quality of the material. We found that all samples investigated show striking inhomogeneity of carrier lifetime on the length scale of 2-7 µm. Although we found inhomogeneity on the same lengths scale using KPFM, interestingly we did not find a

direct correlation between PL and KPFM signal on CIGS films. Additionally, the two-photon excitation capability of our microscopy has allowed us to explore the differences in 1P vs 2P excitation-emission and thus to distinguish bulk vs surface lifetime in CIGS films.

Conclusions

The primary objective of this project was to develop pathways to improve CIGSS modules using precursor reaction processes compatible with low manufacturing cost. Approaches to improve the performance and specifically open circuit voltage of reacted films focused on two material innovations: (1) increasing the overall Ga content from Ga/(In+Ga) ≈ 0.25 as used typically in this process to 0.5 to form reacted films with higher bandgap and V_{OC}, and (2) investigating processing and performance advantages arising from Ag alloying. Fundamental characterization of optoelectronic film properties and advanced device models were used to guide development of H_2Se/H_2S reaction processes including control of relative Ga/In and S/Se profiles for reduced recombination.

The final project milestone was to demonstrate a CIGSS or ACIGSS cell with efficiency ≥ 18% with V_{OC} ≥ 720 mV fabricated using an industrially relevant precursor reaction process that incorporates the advances in gallium content, multi-stage reaction procedures, and silver alloying capabilities developed during the course of the project.

In research on the formation of Cu-Ga-In metal precursors, processes for deposition of precursor stacks using elemental or compound targets were developed. As the Ga/(In+Ga) ratio was increased from 0.25 to 0.5 it was shown how the morphology and phase composition of as-deposited precursors depend on sputter conditions, especially the sputter conditions of the elemental In layer. After inert-atmosphere annealing to mimic the initial heat up phase of any reaction process, it was shown that precursor films with Ga/(In+Ga) = 0.25, 0.35, and 0.5 have comparable phase composition and morphology. This indicates that reaction of higher Ga films will follow from the same starting point as the well-studied lower Ga case. With the addition of Ag to the precursors it was found that the precursor phase composition was not stable on storage at room temperature but could be stabilized by annealing at 300°C. A novel outcome of the precursor studies was the discovery of a new quaternary Laves-type phase in sputter-deposited and evaporated Ag-Cu-In-Ga thin films.

A primary focus was development of processes to react Cu-Ga-In and Ag-Cu-Ga-In sputtered precursors with Ga/(In+Ga) up to 0.5. Systematic study of reaction time-temperature profiles, characterization of phase composition and reaction rates enabled control of composition profiles to engineer bandgap gradients. Reaction analysis with Ag-alloyed precursors to form ACIGS were completed over a complete composition range from 0 ≤ Ag/Cu+Ag) ≤ 1 with the full phase evolution determined. A significant result was that Ag-alloying increases the reaction rate to completely convert precursor films to chalcopyrite during reaction at 450°C. Thus, the incorporation of Ag could be used to reduce reaction time – a potential significant benefit for manufacturing.

A key result was the demonstration of increasing V_{OC} with greater Ga content in the precursor. The highest V_{OC} achieved has been using a 50% Ga precursor, with device parameters V_{OC} = 707 mV, J_{SC} = 27.4 mA/cm^2, FF = 67.3, η = 13.1% (no AR-coating).

High voltage and poor current collection in this device led to the reduction of the Ga content to 40% and the addition of a small amount of Ag to improve adhesion. This led to a device with V_{OC} = 674 mV, J_{SC} = 33.1 mA/cm^2, FF = 71.4%, and η = 16.0% (with AR-coating). The latter gave comparable efficiency but higher V_{OC}.

Device characterization and simulations were used to correlate experimentally measured composition profiles to J-V and QE measurements and guide optimization of composition and bandgap gradients. A critical outcome in all reactions is the front sulfur compositional gradient which can be controlled by the extent of reaction in initial H_2Se reaction stages and, to a lesser extent, the final H_2S reaction. Results from detailed device characterization, including AS, DLCP, and V_{OC} -T measurements, as well as composition-depth profiles were input into numerical simulations to determine an optimized front bandgap gradient. Resulting analyses suggested an increase in near-junction defects with increased S content. Experiments to mitigate this included modification of the final H_2S reaction stage with a lower H_2S concentration. The latter was used to fabricate the highest efficiency device with Ga/(In+Ga) ≥ 0.4. It was also found that conduction band barriers due the S gradient can reduce minority carrier collection resulting in increased voltage dependent collection

The device results above showed the promise of increasing Ga content and Ag-alloying in achieving improved performance and, with process optimization, meeting the final project milestone. However, when the project's industry partner Stion went out of business it was concluded that the long-reaction batch process could no longer be considered commercially relevant. So, for the final budget period the primary focus on reaction and device studies pivoted to development of an RTP process that could potentially be incorporated into a more viable in-line process. In the RTP work, 25% and 50% Ga/(In+Ga) precursors were capped with elemental Se and reacted for 5-15 minutes, compared to typically 2 hours in the batch process. It was shown that competing reaction and evaporation of Se meant that reaction extent is controlled by the amount of Se on the precursor. Films with 50% Ga/(In+Ga) react slower yet produce larger grain films so high Ga films require additional Se thickness to reach desired reaction extents. S was incorporated into films using two approaches, and it was observed that a wide range of S uptake can be achieved by adjusting the S condition and total reaction time. Devices produced with RTP did not achieve comparable performance to films produced with long reactions. A primary reason was identified as film non-uniformity arising from small variations in the RTP heating. But with further optimization and improved heating uniformity, pathways to high quality devices were developed.

Optoelectronic characterization included a focus on development and application of spatial- and time-resolved photoluminescence. A custom IR microscope capable of measuring and mapping photoluminescence and carrier lifetime of CIGS materials and variants was build. By collaborating with several CIGS PV research and development groups we have demonstrated that lifetime strongly depends on the chemical composition and general quality of the material. We found that all samples investigated show striking inhomogeneity of carrier lifetime on the length scale of 2-7 µm. Although we found inhomogeneity on the same lengths scale using KPFM, interestingly we did not find a direct correlation between the PL and KPFM signals on CIGS films. Additionally, the two-

photon excitation capability of our microscopy allowed us to explore the differences in 1P vs 2P excitation-emission and thus to distinguish bulk vs surface lifetime in CIGS films.

The majority of project milestones were successfully met. The BP1 Go/No-Go Decision Point to "Demonstrate a reproducible baseline for solar cell performance using reacted IEC or Stion precursors with average efficiency ≥ 15% and V_{OC} ≥ 620 mV over three consecutive runs" was confirmed using a three-stage $H_2Se/Ar/H_2S$ reaction process on IEC sputtered Cu-Ga-In precursors with Ga/(In+Ga) = 25%. The BP2 Go/No-Go Decision Point to "Demonstrate a CIGSS or ACIGSS device with 17 % efficiency and V_{OC} ≥ 680 mV" was very nearly met as demonstrated by the results listed above using an optimized process with Ga/(In+Ga) = 25% and the V_{OC} target was exceeded with 50% Ga. The BP3 Final Project Milestone to demonstrate a CIGSS or ACIGSS cell with efficiency ≥ 18% with V_{OC} ≥ 720 mV was not achieved. This is attributed to the change in the process under primary investigation due to the re-assessment of commercial viability. This new approach required research to determine critical process control parameters resulting in key insights into the role of a Se capping layer, reaction profile, and heating homogeneity.

Budget and Schedule

The project budget called for a federal share of $800,000 and a cost share of $88,889. These amounts were fully spent with $280,000 spent by the sub-recipient Columbia University. In particular, the cost share was fully met by the prime and sub-recipients.

A budget revision (SF-424a) was applied to the project to enable a six month no-cost extension. This changed the project completion date from 8/31/19 to 2/29/20. This NCE was used to extend support for a UD graduate student working on the project and to more efficiently spend funds in BP3 which had been underspent due to a delayed project start date and an inadvertently slower spend rate in BP2.

Path Forward

The incentive to carry out future research specific to precursor reaction processes for the formation of CIGSS is minimal due to the lack of manufacturing commitment to this process that indicates it is not considered to be a commercially viable approach to thin film PV manufacturing. Consequently, there are also no plans for technology transfer or commercialization resulting from this research project. There are also no patent applications or patents that resulted from the work.

While large scale manufacturing of CIGS using other absorber approaches has lagged in scale-up, several GW of total production in multiple factories is currently being developed overseas and may lead to significant manufacturing cost reductions as they did with Si PV. Thus, maintaining expertise in the US is worthwhile. In addition, CIGS alloys with low bandgap can be utilized as the bottom cell in tandem cells using CdTe-alloy or perovskite top cell. This is a likely basis for future research.

Finally, it is noteworthy that the novel hydride gas reactor at IEC which was utilized and improved in this project has application to other research including the development of novel chalcogenide-based passivation of Si.

Publications Resulting from This Work

1. "Ag–Cu–In–Ga Metal Precursor Thin Films for $(Ag,Cu)(In,Ga)Se_2$ Solar Cells" Sina Soltanmohammad, Lei Chen, Brian McCandless, William N. Shafarman, IEEE Journal of Photovoltaics 7, 273-280 (2017). doi: 10.1109/JPHOTOV.2016.2615682
2. "A quaternary Laves-type phase in Ag-Cu-In-Ga thin films" Sina Soltanmohammad, Brian McCandless, William N. Shafarman, Journal of Alloys and Compounds 710 819-824 (2017). doi: 10.1016/j.jallcom.2017.03.228
3. "Phase Stability in Ag-Cu-In-Ga Metal Precursors for $(Ag,Cu)(In,Ga)Se_2$ Thin Films" Sina Soltanmohammad, Lei Chen, Brian McCandless, William N. Shafarman, Solar Energy Materials & Solar Cells 172, 347–352 (2017). doi: 10.1016/j.solmat.2017.08.009
4. "Reaction Pathway Analysis of $(Ag_xCu_{1-x})(In_{0.75}Ga_{0.25})Se_2$ with x = 0.75 and 1.0" Sina Soltanmohammad and William N. Shafarman, Solar Energy Materials & Solar Cells 182, 142-57 (2018). doi: 10.1016/j.solmat.2017.12.023.
5. "Reaction Rate Enhancement for $Cu(In,Ga)Se_2$ Absorber Materials using Ag-alloying" Sina Soltanmohammad, Ho Ming Tong, Timothy J. Anderson, William N. Shafarman, IEEE Journal of Photovoltaics 9, 898-905 (2019). doi: 10.1109/JPHOTOV.2019.2897582
6. "Investigation of the Electrical Properties of Grain Boundaries in $(Ag_xCu_{1-x})(In_yGa_{1-y})Se_2$" Jake W Wands, Angus A Rockett, Sina Soltanmohammad, William Shafarman, Proc. 46th IEEE Photovoltaic Specialists Conference (Chicago), 962-64 (2019). doi: 10.1109/PVSC40753.2019.8981173
7. "Precursor reaction method with high Ga $Cu(In,Ga)(S,Se)_2$ to achieve increased open-circuit voltage" Isaac K. Lam, Gregory M. Hanket, William N. Shafarman, IEEE Journal of Photovoltaics 10, 1185-1190 (2020). doi: 10.1109/JPHOTOV.2020.2984017
8. "Formation of $Ag(Ga,In)Se_2$ During Selenization Of Ag-Ga/In Precursor" Ho Ming Tong, Sina Soltanmohammad, William N. Shafarman, Timothy J. Anderson, Proc. 47th IEEE Photovoltaic Specialists Conference, 765-1772 (2020). doi: 10.1109/PVSC45281.2020.9300659
9. "Composition Control of High Ga $Cu(In,Ga)(S,Se)_2$ Using RTP Reaction" Isaac K. Lam, Gregory M. Hanket, William N. Shafarman, Proc. 47th IEEE Photovoltaic Specialists Conference, 807-809, (2020). doi: 10.1109/PVSC45281.2020.9300375
10. "Voltage-Induced Charge Redistribution in $Cu(In,Ga)Se_2$ Devices Studied With High-Speed Capacitance-Voltage Profiling" Jeff Bailey, Dmitry Poplavskyy, Geordie Zapalac, Lorelle Mansfield, William Shafarman, IEEE Journal of Photovoltaics. 9, 319-324 (2019). doi: 10.1109/JPHOTOV.2018.2882204
11. "Characterization and Simulation of Electronic Effects of Front Bandgap Gradients in Selenized/Sulfized $Cu(In,Ga)(Se,S)_2$ Solar Cells" Christopher P. Thompson, Isaac Lam, William N. Shafarman, Proc. 7th World Conference on Photovoltaic Energy Conversion (Waikoloa, HI), 2018. doi: 10.1109/PVSC.2018.8547669

Acknowledgments

The following people are thanked for technical contributions to this project (* indicates graduate students supported by the project):

At the University of Delaware: Greg Hanket, Christopher Thompson, Isaac Lam*, Sina Soltanmohhamed*, Wayne Buchanan, Brian McCandless

At Lawrence Berkeley National Lab: Ed Barnard, Ravi Chintala, Paul Ashby

At Columbia University: Peter J. Schuck, Benedikt Ursprung*

At UD we also thank administrative support from Amy Slocum, Susan Tompkins, and Sherry Stewart.

References

[1] Y. Nagoya, K. Kushiya, M. Tachiyuki, O. Yamase, "Role of incorporated sulfur into the surface of $Cu(InGa)Se_2$ thin-film absorber," Solar En Mat Solar Cells 67, 247 (2001). 10.1016/S0927-0248(00)00288-9

[2] K. Kushiya, Y. Tanaka, H. Hakuma, Y..Goushi, S. Kijima, T. Aramoto, Y. Fujiwara. Thin Solid Films 517, 2108 (2009). doi:10.1016/j.tsf.2008.10.125

3 M. Nakamura, K. Yamaguchi, Y. Kimoto, Y. Yasaki, T. Kato and H. Sugimoto, "Cd-Free $Cu(In,Ga)(Se,S)_2$ Thin-Film Solar Cell With Record Efficiency of 23.35%," IEEE Journal of Photovoltaics, 9, 1863-1867 (2019). doi: 10.1109/JPHOTOV.2019.2937218

[4] . Nam, Y. Kang, D. Lee, J. Yang, Y.-S. Kim, C. B. Mo, S. Park, D. Kim, "Achievement of 17.9% efficiency in $30 \times 30\ cm^2$ $Cu(In,Ga)(Se,S)_2$ solar cell sub-module by sulfurization after selenization with Cd-free buffer" Prog. Photovolt: Res. Appl., 24, 175– 182 (2016). doi: 10.1002/pip.2653.

[5] K. Kim, H. Park, G. Hanket, W. Kim, W. Shafarman, "Composition and bandgap control in Cu(In,Ga)Se2-based absorbers formed by reaction of metal precursors" Prog. Photovolt: Res. Appl., 23, 765 (2015). doi: 10.1002/pip.2494

[6] D. Lee, J. Lee, S. Heo, J.-B. Park, Y.-S. Kim, C. B. Mo, K. Huh, J. Yang, J. Nam, D. Baek, S. Park, B. Kim, D. Kim, Y. Kang, "Direct evidence of void passivation in $Cu(InGa)(SSe)_2$ absorber layers,"Appl. Phys. Lett. 106, 083903 (2015); https://doi.org/10.1063/1.4913612

[7] T. Kato , J.-L. Wu , Y. Hirai, H. Sugimoto , V. Bermudez, "Record Efficiency for Thin-Film Polycrystalline Solar Cells Up to 22.9% Achieved by Cs-Treated Cu(In,Ga)(Se,S)2", IEEE J. Photovoltaics, 9, 325 (2019). doi: 10.1109/JPHOTOV.2018.2882206

[8] J. Palm, V. Probst, F.H. Karg, "Second generation CIS solar modules", Sol. Energy 77, 757(2004). doi: 10.1016/j.solener.2004.05.011

[9] M. Algasinger, T. Niesen, T. Dalibor, A. Steigert, R. Klenk, I. Lauermann, R. Schlatmann, M. Ch. Lux-Steiner, J. Palm, "Efficient $Cu(In,Ga)(Se,S)_2$ modules with sputtered Zn(O,S) buffer layer," Thin Solid Films 633, 231 (2017). doi: 10.1016/j.tsf.2016.10.010

[10] G. Hanket, W. Shafarman, B. McCandless, R. Birkmire "Incongruent Reaction of Cu-(InGa) Intermetallic Precursors in H_2Se and H_2S" J Appl Phys 102, 074922 (2007). doi: 10.1063/1.2787151

[11] K. Kim, G. Hanket, T. Huynh, W. Shafarman, Three-step $H_2Se/Ar/H_2S$ reaction of Cu-In-Ga precursors for controlled composition and adhesion of $Cu(In,Ga)(Se,S)_2$ thin films" J Appl. Phys. 111, 83710 (2012). doi: 10.1063/1.4704390

[12] Y. Tauchi, K. Kim, H. Park, W .Shafarman, "Characterization of $(AgCu)(InGa)Se_2$ Absorber Layer Fabricated by Selenization Process from Metal Precursor" IEEE J Photovoltaics 3, 467 (2013). doi: 10.1109/JPHOTOV.2012.2221083

[13] S. Soltanmohammad, L. Chen, B. McCandless, W. Shafarman, "Ag–Cu–In–Ga Metal Precursor Thin Films for $(Ag,Cu)(In,Ga)Se_2$ Solar Cells", IEEE Journal of Photovoltaics 7, 273-280 (2017). doi: 10.1109/JPHOTOV.2016.2615682

[14] S. Soltanmohammad, L. Chen, B. McCandless, W. Shafarman, "Phase Stability in Ag-Cu-In-Ga Metal Precursors for $(Ag,Cu)(In,Ga)Se_2$ Thin Films" Solar Energy Mats & Solar Cells 172, 347–352 (2017). doi: 10.1016/j.solmat.2017.08.009

[15] S. Soltanmohammad, B. McCandless, W. Shafarman, "A quaternary Laves-type phase in Ag-Cu-In-Ga thin films" Journal of Alloys and Compounds 710, 819-824 (2017). doi: 10.1016/j.jallcom.2017.03.228

[16] S. Soltanmohammad, W.N. Shafarman, Reaction pathway analysis of Ag-alloyed $Cu(In,Ga)Se_2$ absorber materials" Proc. IEEE 43rd Photovoltaic Specialist Conference, 2269 (2017). doi: 10.1109/PVSC.2016.7750040

[17] C. Thompson, D. Lee and W. N. Shafarman, "Characterization and numerical modeling of $Cu(In,Ga)(S,Se)_2$ solar cells," 42nd Photovoltaic Specialist Conference, IEEE, New Orleans, 2015. doi: 10.1109/PVSC.2015.7355775

[18] M. Burgelman, P. Nollet and S. Degrave, "Modelling polycrystalline semiconductor solar cells," Thin Solid Films, Vols. 361-362, pp. 527-532 (2000). doi: 10.1016/S0040-6090(99)00825-1

[19] S.S. Hegedus and W.N. Shafarman, "Thin Film Solar Cells: Device Measurements and Analysis," *Progress in Photovoltaics* **12**, 155 (2004). doi: 10.1002/pip.518

[20] J. T. Heath, J. D. Cohen and W. N. Shafarman, "Bulk and metastable defects in CuIn1-xGaxSe_2 thin films using drive-level capacitance profiling," J. Appl. Phys., vol. 95, no. 3, pp. 1000-1010, 2004. doi: 10.1016/S0040-6090(99)00825-1

[21] M. Bar, W. Bohne, J. Rohrich, E. Strub, S. Lindner, M. C. Lux-Steiner, C. H. Fischer, T. P. Niesen and F. Karg, "Determination of the band gap depth profile of the penternary $Cu(In_{1-x}Ga_x)S_YSe_{Y-1})_2$ chalcopyrite from its composition gradient," Journal of Applied Physics, no. 96, pp. 3857-3860, 2004. doi: 10.1063/1.1786340

[22] R. Lovelett, G. Hanket, W. Shafarman, R. Birkmire, B. Ogunnaike, "Design and experimental implementation of an effective control system for thin film $Cu(InGa)Se_2$ production via rapid thermal processing", Journal of Process Control 46 24–33 (2016). doi: 10.1016/j.jprocont.2016.07.005

[23] E. Barnard et al., "Three-Dimensional Lifetime Tomography Reveals How CdCl2 Improves Recombination Throughout CdTe Solar Cells," Adv. Mater. 2016. doi: 10.1002/adma.201603801

[24] C. Walkons, M. Jahandardoos, T. Friedlmeier, W. Hempel, O. Salomon, M. Nardone, Y. Patikirige, B. Ursprung, E. Barnard, K. Kweon, V. Lordi, S. Bansal. "Behavior of Na and RbF-Treated CdS/Cu(In,Ga)Se2 Solar Cells with Stress Testing under Heat, Light, and Junction Bias" Submitted March 2020

[25] P. T. Erslev, W. N. Shafarman, and J. D. Cohen, "Metastable properties of Cu(In1−xGax)Se2 with and without sodium," Appl. Phys. Lett., vol. 98, no. 6, p. 062105, Feb. 2011, doi: 10.1063/1.3553783.